

*Digital Comprehensive Summaries of Uppsala Dissertations
from the Faculty of Science and Technology 2308*

Interfacial Analysis and Charge Transfer in Solar Cells

XINJIAN GENG



ACTA UNIVERSITATIS
UPSALIENSIS
2023

ISSN 1651-6214
ISBN 978-91-513-1900-1
urn:nbn:se:uu:diva-512175



UPPSALA
UNIVERSITET

Dissertation presented at Uppsala University to be publicly examined in Polhemsalen, Ångströmlaboratoriet, Lägerhyddsvägen 1, Uppsala, Friday, 10 November 2023 at 10:15 for the degree of Doctor of Philosophy. The examination will be conducted in English. Faculty examiner: Professor Ellen Moons (Department of Engineering and Physics, Karlstad University).

Abstract

Geng, X. 2023. Interfacial Analysis and Charge Transfer in Solar Cells. *Digital Comprehensive Summaries of Uppsala Dissertations from the Faculty of Science and Technology* 2308. 67 pp. Uppsala: Acta Universitatis Upsaliensis. ISBN 978-91-513-1900-1.

Harnessing sunlight through solar cells is vital for sustainable energy production. The conventional architecture of a solar cell consists of multilayers of materials, each serving a particular function. The absorbing layer converts the solar energy into valuable electricity by the photovoltaic effect. Positioned on either side of the absorbing layer are charge transport layers, which collect the generated electricity. Charge transfer and recombination occur at interfaces, affecting the solar cells' open-circuit voltage (V_{oc}). This doctoral thesis focuses on the analysis of the perovskite/n-type semiconductor interface and plasmonic/p-type semiconductor interface, provides an understanding of the charge generation and transfer in solar cells, and helps to establish a selection of the ideal charge transport layer for efficient charge extraction.

Initially, photogenerated charge carriers were investigated by time- and energy-resolved photoluminescence (TER-PL) from the thin formamidinium lead-bromide (FAPbBr₃) perovskite absorber film. Both exciton and free charge dynamics under various excitation power intensities were taken into consideration. Following studies on the charge transfer at interfaces were performed by incorporating n-type semiconductors (TiO₂ and SnO₂) as the charge transport layer. The results revealed that the TiO₂ is more efficient as a fluorescence quencher due to the higher density of states in its conduction band. While conductivity measurements suggested that SnO₂ was better for avoiding the accumulation of charges. Thus, solely charge extraction efficiency is not sufficient for determining the solar cell performance.

To alleviate the energy losses in solar cells, extraction of hot electrons would be a viable way. Then, hot carriers generated through plasmon excitation in metal nanoparticles, which is different from semiconductors, were collected in the solid-state direct plasmonic solar cell (DPSC). Also, plasmonics show high absorption across the visible–infrared spectrum. Early progress mainly focused on hot electron transfer. The second part of the thesis investigated the effect of Li-TFSI dopant concentration in the hole transport layer (spiro-OMeTAD) on solar cell performance. 33% oxidised species (spiro⁺TFSI⁻) gave the optimal efficiency. By using transient absorption spectroscopy, the injection of hot electrons and holes was verified in a complete solar cell device as well.

Keywords: Perovskites, Charge Transport Layer, Plasmonics, Hot Carriers, Interfaces, Photoluminescence, Solar Cells

Xinjian Geng, Department of Chemistry - Ångström, Physical Chemistry, Box 523, Uppsala University, SE-75120 Uppsala, Sweden.

© Xinjian Geng 2023

ISSN 1651-6214

ISBN 978-91-513-1900-1

URN urn:nbn:se:uu:diva-512175 (<http://urn.kb.se/resolve?urn=urn:nbn:se:uu:diva-512175>)

*Logic will get you from A to Z.
Imagination will get you everywhere.
- Albert Einstein*

List of papers

This thesis is based on the following papers, which are referred to in the text by their Roman numerals.

- I **Transient Energy-Resolved Photoluminescence Study of Excitons and Free Carriers on FAPbBr₃ and FAPbBr₃/SnO₂ Interfaces**
Xinjian Geng, Yawen Liu, Xianshao Zou, Erik M. J. Johansson, and Jacinto Sá*
J. Phys. Chem. C, 2023, 127, 6, 3085-3092.
- II **Can Photoluminescence Quenching Be a Predictor for Perovskite Solar Cell Efficiencies?**
Xinjian Geng, Yawen Liu, Xianshao Zou, Erik M. J. Johansson, and Jacinto Sá*
Phys. Chem. Chem. Phys., 2023, 25, 22607-22613.
- III **Direct Plasmonic Solar Cell Efficiency Dependence on Spiro-OMeTAD Li-TFSI Content**
Xinjian Geng, Mohamed Abdellah, Robert Bericat Vadell, Matilda Folkenant, Tomas Edvinsson, and Jacinto Sá*
Nanomaterials, 2021, 11, 3329.
- IV **Ultrafast Infrared-to-Visible Photon Upconversion on Plasmon/TiO₂ Solid Films**
Xianshao Zou, Robert Bericat Vadell, Bin Cai, Xinjian Geng, Ananta Dey, Yawen Liu, Axel Gudmundsson, Jie Meng, and Jacinto Sá*
J. Phys. Chem. Lett. 2023, 14, 27, 6255-6262.

Reprints were made with permission from the publishers.

Contribution Report

- I Prepared the metal oxide semiconductor films and carried out the photoluminescence measurements. Performed the transient photoluminescence spectroscopy with Xianshao's assistance. Analyzed the data and provided the figures and tables. Supported in the revising process.
- II Prepared the metal oxide semiconductor films. Performed the transient photoluminescence spectroscopy with Xianshao's assistance. Fabricated devices and performed the conductance measurement. Analyzed the data, and provided all the figures and tables. Wrote the first draft of the manuscript (sections: abstract, methods, and results and discussion).
- III Prepared samples for characterizations: scanning electron microscopy and transient absorption spectroscopy. Conducted the data fitting. Fabricated solar cells and performed the rest of the characterizations: current-voltage measurement, quantum efficiency, and Raman spectroscopy. Analyzed all of the data and provided figures and tables.
- IV Participated in the transient photoluminescence measurements.

Contents

1	Introduction	9
1.1	Solar Energy	9
1.2	Types of Solar Cells	9
1.3	The Shockley-Queisser Limit	10
1.4	Harvest Hot Carriers	11
1.5	Aims and Outline	12
2	Theory	13
2.1	Photophysics of Materials	14
2.1.1	Semiconductor	14
2.1.2	Plasmonics	19
2.2	Physics of Solar Cell Devices	20
2.2.1	Interfaces	20
2.2.2	Charge Injection	21
3	Methods	23
3.1	Materials Preparation	23
3.1.1	Synthesis of the Au Nanoparticle	23
3.1.2	Preparation of Semiconductor Films	23
3.2	Scanning Electron Microscope (SEM)	24
3.3	Optical Characterization	24
3.3.1	UV-vis Spectrophotometer	24
3.3.2	Raman Spectroscopy	26
3.3.3	Photoluminescence (PL) Spectroscopy	27
3.3.4	Femtosecond Transient Absorption Spectroscopy	28
3.4	Device Characterization of Solar Cells	29
3.4.1	Current-Voltage (I-V) Measurement	29
3.4.2	Quantum Efficiency	30
3.5	Conductivity	31
4	Electron Transport Layer/FAPbBr ₃ Interface in the Perovskite Solar Cell (Paper I and II)	32
4.1	Photoluminescence of the FAPbBr ₃ Film	33
4.2	TiO ₂ vs SnO ₂	36
4.3	Modification of the SnO ₂ ETL	39
4.4	Conclusion	42
5	Interfaces in the Direct Plasmonic Solar Cell (Paper III and IV)	43
5.1	Direct Plasmonic Solar Cell	44

5.2	Dopant Concentration in Spiro-OMeTAD	45
5.3	Absorption Enhancement	47
5.4	Conclusion	48
6	Summary and Outlook	50
7	Popular Scientific Summary	53
8	Populärvetenskaplig Sammanfattning	55
9	Acknowledgements	57
	References	59

1. Introduction

1.1 Solar Energy

The demand for energy is increasing, ranging from residential, commercial, transportation, and industrial consumption. To improve energy efficiency, old and inefficient equipment has been replaced with advanced and energy-efficient devices. However, that is not sufficient to suppress the energy demands and achieve net zero emissions. We need to accelerate the transition from fossil fuels to renewable green energy, in particular, derived from wind and sunlight.

Regarding electricity generation, conventional technologies such as coal- and nature-gas-fired electricity are based on the conversion of thermal energy or heat energy of gas to electricity via steam and combustion turbines. Other turbine-driven generators, such as hydroelectric turbines, wind turbines, and ocean thermal energy conversion systems, convert renewable resources into electricity. Considering the significant amount of solar energy that can potentially be captured (around 4375-13843 PWh per year) [1], solar energy is by far the largest energy resource on Earth. With the aid of concentrated solar power (CSP) systems, solar energy also can be converted into thermal energy, driving a steam engine to generate electricity. Certain CSP technologies can be integrated into fossil fuel power plants, decreasing carbon emissions and maximizing efficiency during the process of both resources.

Compared with other types of solar energy conversion technology, solar cells or solar photovoltaics (PV) directly convert sunlight into electricity at a lower cost. Recently, studies of cities' solar-generated electricity in China have proved that the grid-connected solar PV system could supply electricity at the same price as grid-supplied desulfurized coal electricity or even lower [2]. Hence, grid parity is highly possible to be achieved in solar PV power systems. Not only direct sunlight, indoor lights with lower intensity, and only the visible spectrum could also be the light source for solar cells. As a result, investments in solar cells are reliable and environment-friendly.

1.2 Types of Solar Cells

The photovoltaic effect was observed in devices with an asymmetric interface structure that can drag photon-excited electrons to an external circuit. In the 1950s, the manufacturing of p-n junction was realized in silicon. Basically,

the surface of n-type silicon (Si) wafers was converted to a p-type when exposed to the boron trichloride gas. By etching part of the p-type surface, the n-type layer beneath was exposed. This p-n junction structure was then used to fabricate the silicon solar cell. Two main disadvantages of the silicon solar cell are the requirement for a high-quality silicon layer and great thickness (over 100 μm). To lower the cost during the processing steps, polycrystalline Si, amorphous Si, and stacked amorphous/polycrystalline Si are used to manufacture solar cells. In addition, thin-film technologies have been developed when using alternative absorbing materials such as Cu(In,Ga)(Se,S)_2 (CIGS) and CdTe. Recently, emerging thin-film solar cells employing organic semiconductors, quantum dots, and perovskites have attracted attention because the electronic and optical properties of absorbing materials can be easily tuned by altering the molecular structure of the materials. Especially, much of the spotlight has been on solution-processable perovskites for their potential in fabricating large-area thin films at a low cost. Tandem solar cells by stacking silicon and perovskite solar cells have been successful in reaching higher efficiencies.

A common structure exists among the mentioned single-junction solar cells. The built-in p-n junction is necessary to pull the excited electrons away from holes and contributes to the potential difference. In some highly efficient solar cells, extra charge transport layers are employed to selectively extract and transport electrons (holes) and prevent holes (electrons) for the purpose of reducing recombination and reverse transfer. A good charge transport layer should prevent losses during charge extraction and facilitate charge collection. Therefore, this thesis focuses on the interaction between the charge transport layer and the absorbing layer for the purpose of providing information on selecting suitable charge transport materials.

1.3 The Shockley-Queisser Limit

In a single semiconductor solar cell under one sun illumination, losses resulting from series and parasitic resistances can substantially limit its efficiency. However, these are not considered when calculating fundamental limiting efficiency. Intrinsic losses are unavoidable even in ideal solar cells as shown in Figure 1.1a [3]. They are (1) unabsorbed photons with energy below the semiconductor bandgap (E_g loss); (2) highly energetic carriers cool to the bottom of the conduction band via collisions with the lattice (thermalization loss), (3) radiative recombination with photon emission (emission loss), (4) heat conduction and convection with the cold environment (Carnot loss), and (5) mismatch of absorption and emission angles (Boltzmann loss). With theoretical calculation, the maximum solar conversion efficiency is around 33.7% achieved in a single p-n junction with a band gap of 1.4 eV.

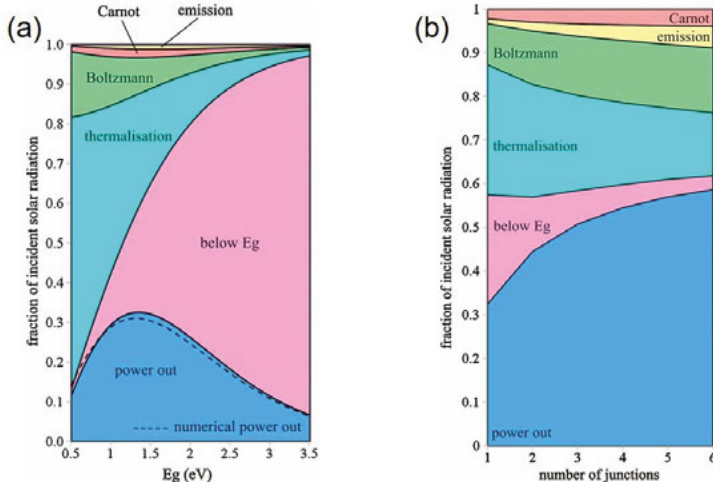


Figure 1.1. (a) Losses and power out in (a) a single junction solar cell; (b) an unconstrained multijunction solar cell under one sun illumination. Reprinted with permission from Hirst et al., *Progress in Photovoltaics: Research and Applications*, 19(3):286-293, 2011 [3]. Copyright 2010 John Wiley and Sons.

To avoid some losses, multijunction solar cells have been conceived. Energy losses are presented in Figure 1.1b. Thermalization loss in multijunction solar cells is reduced. An example of the tandem solar cell is fabricated by stacking silicon and perovskite solar cells which have succeeded in reaching a higher efficiency of over 30% [4]. Due to the complicated device structure, the fabrication of tandem solar cells is still a big challenge.

1.4 Harvest Hot Carriers

Another advanced solar cell device that can limit thermalization loss is the hot carrier solar cell. Hot carriers are produced when the incident photons with energies that are significantly larger than the semiconductor's bandgap. The efficiency of the hot carrier solar cell can reach up to 66% theoretically [5]. And only three layers, an absorbing layer and two charge transporting layers, are needed to construct the solar cell, superior to the complex tandem solar cell structure.

On the other hand, the excitation of plasmons in metallic nanostructures (for example Au, Ag, and Cu) can also generate hot carriers. The timescale of hot carrier generation and following transfer to semiconductors before the thermal equilibration ranges from femtoseconds to picoseconds (<10 ps). Therefore, it is challenging to collect hot carriers efficiently in solar cell devices. One strategy is to employ a suitable charge transport layer to strengthen the coupling

between the plasmonic nanoparticle and the semiconductor and accelerate the charge extraction.

1.5 Aims and Outline

Herbert Kroemer, who received the Nobel Prize in Physics in 2000 for developing semiconductor heterostructures used in high-speed- and opto-electronics, stated that **“the interface is the device”** [6]. Charge transfer happens at the interface. Thus, the interaction between adjacent layers plays an important role in the working principle of devices, and understanding the interface helps us to find strategies to increase device efficiency.

This thesis focuses on the charge transfer behaviors in perovskite solar cells and direct plasmonic solar cells. Also, the effect of the properties of charge transport layers on charge transportation has been studied. Questions that the thesis attempted to answer are listed below.

In large-bandgap perovskites:

- Are bounded excitons involved in the electron transfer process?
- Can transient photoluminescence measurements be used to predict perovskite solar cell efficiencies without additional measurements?
- Can power-dependent transient photoluminescence measurements provide additional information on perovskite interaction with light?

In plasmonics:

- Can we quantify the effect of hole transport layer doping concentration on solar cell performance?
- Is the plasmonic effect related to only hot carrier generation or can it also have a photonic effect?

2. Theory

Light is viewed as an electromagnetic wave having both electric and magnetic fields as illustrated in Figure 2.1. Light can also be considered to be made up of particles referring to photons. The energy of one photon (E) is related to the wavelength (λ) as described in the equation:

$$E = h\nu = hc/\lambda \quad (2.1)$$

where h is the Planck's constant, ν is the frequency, and c is the speed of light.

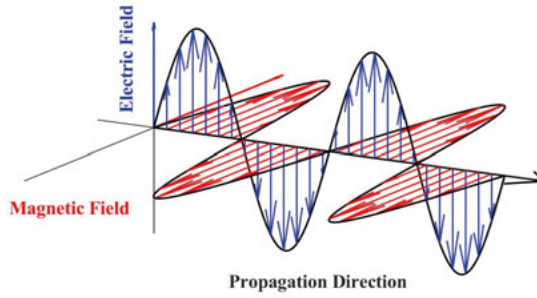


Figure 2.1. An electromagnetic wave containing one magnetic field (red) and one electric field (blue).

When incident light interacts with the optical material, the following phenomena can be classified into three optical processes: reflection, propagation, and transmission. Furthermore, refraction, absorption, luminescence, and scattering occur as light propagates through the material. In the submicroscopic view, atoms are assembled together to form matter. And in an atom, many electrons and one neutron exist. In the classical model, an electron (negative) and a nucleus (positive) form a dipole and the binding interaction between them is compared to a spring. Therefore, the coupling of dipole oscillators in matter to the electromagnetic radiation field determines these optical properties. Taking the collision processes among atoms into consideration, the decay of oscillation happens. As a consequence, the incident light frequency, coupling strength, and damping rate are related to the amplitude of these oscillations. In semiconductor materials, many bound electrons exist and there is a restoring force when they are relocated (related to the spring constant). The damped harmonic oscillator works for the interaction between light and

bound electrons. While significant numbers of electrons are free to move in metals, the spring constant is zero and the Drude-Lorentz model is applied to free electron oscillators. This will help to explain the plasmonic properties of metal nanoparticles mentioned in the following part.

2.1 Photophysics of Materials

2.1.1 Semiconductor

In the semiconductor, the valence band (VB) contains electrons, and the band of unoccupied orbitals is known as the conduction band (CB). If the positions of the conduction band minimum and the valence band minimum are at the same wave vector (k) (Figure 2.2a) in the Brillouin zone, the semiconductor has a direct band gap. If they occur at different wave vectors, the semiconductor has an indirect band gap (Figure 2.2b). In this section, the optical transitions in direct band gap semiconductors are discussed.

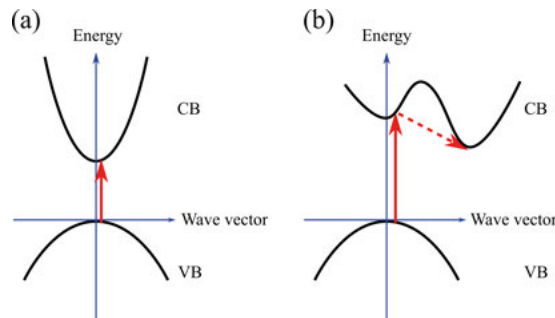


Figure 2.2. Band structures in semiconductors: (a) direct band gap, (b) indirect band gap. The red vertical arrow represents the photon absorption process and the dashed arrow represents the emission of a phonon.

Absorption processes

Light absorption is an essential process for the generation of charge carriers in solar cells. After the absorption of photons by a semiconductor, electrons will be excited from a low-energy state to a high-energy state. This electron transition can take place between two bands or through defect states, as shown in Figure 2.3. When the photon energy ($h\nu$) is higher than the semiconductor band gap energy (E_g), an electron is excited from the valence band to the conduction band (processes a and b). When the photon energy is less than the band gap, the electronic transition can be achieved through defect states (donor or acceptor) within the forbidden gap (processes c, d, and e). Intersubband absorption (process f) can also occur at much lower photon energies.

Absorption coefficient (α) is a parameter used to quantify the photon absorption by a material. The value of α is closely related to the possibility for

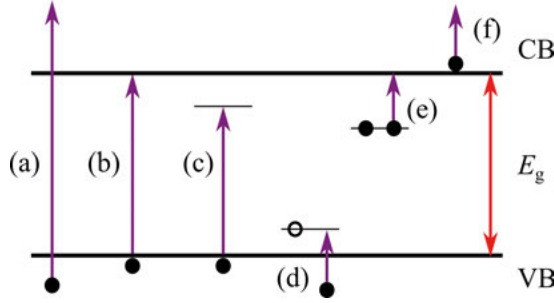


Figure 2.3. Absorption processes: (a) $h\nu > E_g$, (b) $h\nu = E_g$, (c) the valence band to donor levels, (d) acceptor level to the valence band, (e) donor level to the conduction band, (f) interconduction band.

the transition and the number of possible transitions which could be evaluated by the density of states. For valence-conduction band transitions in a direct band gap semiconductor, the expression for α_{vc} is [7]

$$\alpha_{vc}(h\nu) = A^*(h\nu - E_g)^{1/2} \quad (2.2)$$

where A^* is correlated with the index of refraction and effective masses of electrons and holes. Due to the low density of defect states involved in optical transitions, such defect absorption coefficient (α_d) is normally very small. It declines exponentially and can be expressed as [8]

$$\alpha_d = \alpha_0 \exp\left(\frac{h\nu - E_g}{E_0}\right) \quad (2.3)$$

Here, α_0 and E_0 are empirical parameters depending on the semiconductor and its defects related to preparation, doping, and various treatments. This dependence of the optical absorption is commonly observed and is referred to as the Urbach tail [9].

As for the formamidinium lead-bromide (FAPbBr₃) perovskite, direct optical transition exists and the absorption coefficient has values between 10^5 cm^{-1} and 10^6 cm^{-1} when photon energies are larger than the bandgap (about 2.2 eV) [10].

Excitons and free charges

The band-to-band absorption discussed in the previous section assumes that the electron is fully delocalized and the interaction between electrons is neglected. For some semiconductors characterized by an excellent local screening of the free-carrier interaction (large relative dielectric constant), this approximation works well. While for other semiconductors such as organic-inorganic hybrid perovskite semiconductors, the Coulomb attraction can prompt the formation of the bound electron-hole pair. This is termed an exciton, a quasi-particle involved in electronic excitation. There are two basic types:

Wannier-Mott exciton and Frenkel exciton. The Wannier-Mott exciton has a large separation of the electron and the hole that encompasses many atoms. Hence, they are delocalized states and also called the free exciton. Conversely, the Frenkel exciton has a much smaller radius and is tightly bounded to specific atoms.

The free exciton can be modeled as a hydrogenic system. The bound states are characterized by the principle quantum number n , and the binding energy of the n th level relative to the ionization limit is given by [11]:

$$E_B(n) = -\frac{\mu}{m_0} \frac{1}{\epsilon_r^2} \frac{R_H}{n^2} = -\frac{R_X}{n^2} \quad (2.4)$$

where μ is the reduced mass, m_0 is the electron mass, R_H is the Rydberg energy of the hydrogen atom (13.6 eV) and ϵ_r is the dielectric constant. Excitonic absorption can be achieved during the direct optical transitions between the valence and conduction bands. And the energy of the exciton is calculated from the energy required to create the electron-hole pair (E_g) and the binding energy due to the Coulomb interaction (eqn.2.4). As a result, the energy of n th excitonic level is expressed by:

$$E(n) = E_g - \frac{R_X}{n^2} \quad (2.5)$$

We could imagine that excitons will be easily broken up into free carriers if their binding energy is much lower than the thermal energy, $k_B T$. Besides the thermal energy, the total density of particles in the system is another crucial variable to be considered. The system consists of free carriers and excitons that are in thermodynamic equilibrium. This implies a balance between dissociation and recombination events. When the free carrier density is very low, the probability of regenerating an exciton from the dissociated state is very small in spite of the binding energy exceeding $k_B T$. However, if the binding energy is much larger than $k_B T$, there will be a stable exciton population even at a low free carrier density. Such phenomenon is described by the Saha-Langmuir equation [12]:

$$\frac{x^2}{(1-x)} = \frac{1}{n} \left(\frac{2\pi\mu k_B T}{h^2} \right)^{3/2} e^{\frac{-E_B}{k_B T}} \quad (2.6)$$

where x is the fraction of free carriers (n_{eh}/n), n is the total number of particles (related to the excitation density), and μ is the exciton reduced mass:

$$\mu = \frac{m_e^* + m_h^*}{m_e^* * m_h^*} \quad (2.7)$$

where m_e^* and m_h^* are the effective masses for electrons and holes.

An intuitive picture of the shape of this equation: the higher the temperature the greater the free carrier ratio due to the improved ionization process, but as the excitation density increases the possibility of electron-hole interaction with subsequent exciton formation prevails and the ratio is reduced.

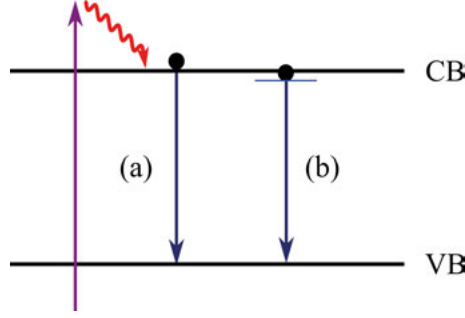


Figure 2.4. Simplified picture of the recombination processes: (a) band-to-band recombination, (b) exciton state recombination. The red curved arrow represents the relaxation before recombination.

Recombination processes

After the absorption of photon energy ($h\nu > E_g$), charge carriers are not in thermal dynamic equilibrium instantaneously. The first ultrafast process is an elastic scattering between the carriers which occurs within 100 fs after the excitation [13]. At this stage, the total energy of the carrier population is conserved, and the energy exchange between carriers results in the Fermi-Dirac distribution at a temperature higher than the lattice temperature. Subsequently, a cooling process of the charge carrier occurs through carrier-phonon scattering within 100 fs to 1 ps. Slower cooling processes (up to about 10 ps) have also been observed in $\text{CH}_3\text{NH}_3\text{PbI}_{3-x}\text{Cl}_x$ semiconductor films. In consequence, the excess energy is quickly lost as heat during the relaxation of the excited carriers to the edges of valence and conduction bands. Such relaxation events take place faster than the recombination process.

Being the reverse process of photogeneration of mobile electrons and holes, recombination leads to the reduction of charge carrier concentration in semiconductors. Excited electrons will decay to a lower energy state with the energy released either as photons (radiative recombination) or heat through phonon emission (non-radiative recombination). Fundamental transitions occurring at or near the band edge are considered here (Figure 2.4). In the band-to-band recombination, electrons fall directly from the conduction band to the valence band. Since the radiative recombination rate could be expressed in terms of the carrier densities, it would be useful to study the charge carrier transfer at interfaces by the luminescence intensity.

When excitons are generated, their concentration n is expressed as:

$$\frac{dn}{dt} = G - \frac{n}{\tau_r} - \frac{n}{\tau_{nr}} = G - \frac{n}{\tau} \quad (2.8)$$

where G is the generation, τ_r is the radiative recombination time, and τ_{nr} is the non-radiative recombination time. When the optical excitation is switched off

($G = 0$) at time $t = 0$, equation (2.8) changes into

$$\frac{dn}{dt} = -\frac{n}{\tau} \quad (2.9)$$

and its solution is

$$n(t) = n(0)\exp(-t/\tau) \quad (2.10)$$

The luminescence intensity (the number of photons emitted from unit volume per unit time) is given by the ratio $n(t)/\tau_r$, and hence the intensity decay is

$$i(t) = \frac{n(t)}{\tau_r} = \frac{n(0)}{\tau_r} e^{-t/\tau} = i(0)e^{-t/\tau} \quad (2.11)$$

We can see that in the exciton recombination process, the luminescence exhibits strictly single-exponential decay. Those functions above described can also be used for the trap-assisted recombination process. In trap-assisted recombination, an electron and a hole will be annihilated when captured by a trap state together. It can happen either in the bulk of a semiconductor or on the interface.

When free electrons and holes are produced, electrons and holes will diffuse along the edges of the respective bands, and eventually, electrons will encounter and recombine with the nearest holes whether radiatively or non-radiatively. The processes are described by the equation [14]:

$$\frac{dn(t)}{dt} = G - \beta np = G - \beta n^2 \quad (2.12)$$

where n and p represent the concentrations of electrons and holes respectively. The coefficient β is called the bimolecular recombination coefficient and can be expressed as the sum of radiative (β_r) and non-radiative (β_{nr}) recombination coefficients. The solution of equation (2.12) is

$$n(t) = \sqrt{\frac{G}{\beta}} \frac{1 - e^{-2\sqrt{G\beta}t}}{1 + e^{-2\sqrt{G\beta}t}} + \text{const.} \quad (2.13)$$

Since the excitation pulse is sufficiently short, $2\sqrt{G\beta}t \ll 1$, then we can approximately get $n(t) \approx Gt$. Then, the luminescence intensity $i(t) = \beta_r n^2(t)$ is given by

$$i(t) = \beta_r n^2(t) \approx \beta_r G^2 t^2 \approx \beta_r \alpha^2 t^2 I_{\text{ex}}^2 \quad (2.14)$$

in which the generation G is replaced with the multiplication of the excitation intensity (I_{ex}) and absorption coefficient (α). Hence, the intensity of the luminescence under laser pulse excitation is proportional to the square of the excitation intensity I_{ex} .

Another recombination mechanism is the Auger recombination. In this process, the energy released by a band-to-band transition or trap-assisted transition will give rise to the excited free electron in the conduction band. This

high-energy electron will lose its energy while colliding with the lattice and finally relaxes to the conduction band. Auger recombination usually happens in degenerate semiconductors or a high-level excitation condition where free carriers are in high concentration.

2.1.2 Plasmonics

Localized surface Plasmons

Localized surface plasmon resonance (LSPR) is an interesting phenomenon occurring on the surface of metal nanostructures. When electromagnetic radiation of an appropriate wavelength illuminates on a gold nanostructure, the displaced electron cloud of the metal will begin to oscillate collectively relative to the nuclei with the frequency of the incoming light. Figure 2.5 demonstrates this phenomenon for a gold nanoparticle. When light is illuminated on the particle, two interactions occur namely scattering and absorption. In the scattering process the incoming light is re-radiated in all directions at the same wavelength while in the absorption process, the energy is absorbed and converted into vibrations of the lattice (i.e. phonons). In total, these two processes are referred to as extinction (extinction = absorption + scattering) [15]. When the frequency of light matches with the intrinsic frequency of the nanoparticle a resonance condition will occur, which is localized surface plasmon resonance. The resonance frequency (or wavelength) of plasmonic nanoparticles depends on many factors including size, shape, composition, inter-particle distance, medium, etc.

In the case of spherical nanoparticles, the diameter D of the particle has a significant impact on the absorption and scattering cross-sections. Specifically, the absorption cross-section increases with D^3 and the scattering cross-section increases with D^6 . For particles smaller than 30 nm, the contributions to optical phenomena are mainly dominated by absorption instead of scattering. Thus, the extinction cross-section is approximately equivalent to the absorption cross-section [16]:

$$\sigma_{\text{abs}} = \frac{9V\epsilon_m^{3/2}}{c} \frac{\omega\epsilon_2(\omega)}{[\epsilon_1(\omega) + 2\epsilon_m]^2 + \epsilon_2(\omega)^2} \quad (2.15)$$

where ω is the angular frequency of light, V is the volume of particle, c is the speed of light, ϵ_m is the real part of the permittivity of surrounding medium and $\epsilon_1(\omega)$, $\epsilon_2(\omega)$ are the angular frequency dependent real and imaginary parts of the dielectric function, respectively. The intensity of the plasma resonance is very high and the extinction coefficient of a gold nanoparticle with a core size of 10 nm is about $9.4 \times 10^7 M^{-1} cm^{-1}$ [17] [18].

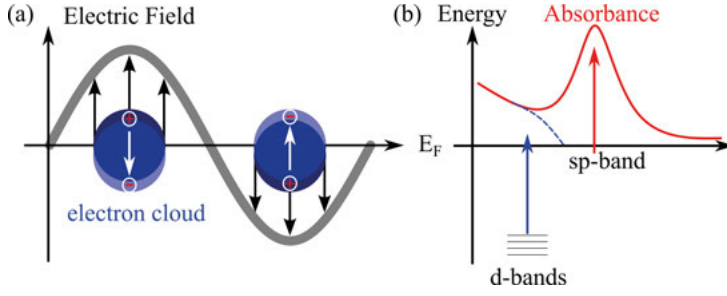


Figure 2.5. Surface plasmon resonance: (a) electromagnetic wave induced electron cloud displacements in nanoparticles, (b) illustration of the interband (blue arrow) and intraband (red arrow) transitions in gold nanoparticles, and the corresponding absorbance spectrum.

Hot-carrier generation

Once excited, plasmons can lose their energy either radiatively (photoluminescence by emitting a photon) or non-radiatively, by generating an electron-hole pair within the metal conduction band. Experimental findings explain a process in which excited d-band holes recombine non-radiatively with sp electrons, emitting particle plasmons (PPs). These plasmons subsequently radiate, giving rise to the observed photoluminescence [19].

The phenomenon, known as Landau damping, leads to the creation of a hot-electron population [20], characterized by a temperature exceeding that of the lattice and affected by the plasmonic resonance. The efficiency of the Landau damping mechanism, along with the associated dynamics, strongly relies on factors such as nanoparticle material, size, shape, and environment. Once excited, this population of hot-electron, which is out of equilibrium, thermalizes at a given effective temperature distribution, that could be described by Fermi- or approximated by Maxwell-Boltzmann-statistics, via electron-electron scattering [21]. These interactions typically take place within hundreds of femtoseconds. Simultaneously, heat is transferred into the crystal lattice through electron-phonon inelastic scattering within 3-5 ps. Moreover, the lifetime of out-of-equilibrium electrons in metal nanoparticles varies with their energy and is inversely proportional to $(E - E_F)^2$ [22] [23].

2.2 Physics of Solar Cell Devices

2.2.1 Interfaces

To harvest the hot-electron population, one must collect the excited electrons before thermalization. This means that electrons, which are only driven by their thermal motion, need to reach the metal interface in a fast timescale and retain high enough kinetic energy so they can be extracted. As they move, excited electrons can undergo several scattering events with other free electrons

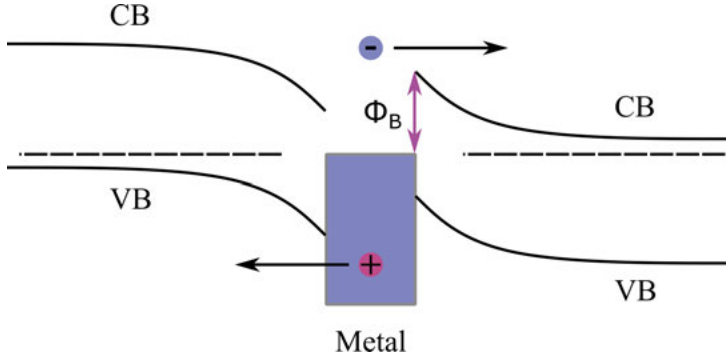


Figure 2.6. semiconductor (p-type)-metal-semiconductor (n-type) architecture for hot electron harvesting.

in the metal. The average distance traveled by an electron before electron and phonon scattering resulting in thermalization is the so-called electron mean free path (L_{MFP}) [24], which can be calculated according to the lifetime and group velocity of electronic state. This quantity depends both on the material properties and on the electron energy. For all metals, previous observations revealed that low-energy carriers situated near the Fermi level exhibit the longest lifetimes and mean free paths. Similar maximum carrier lifetimes of approximately 30 femtoseconds (fs) and mean free paths of roughly 50 nanometers (nm) were observed among noble metals, with the order being $Ag > Cu > Au$. In contrast, aluminum (Al) exhibits a smaller maximum lifetime of around 10 fs and a mean free path of approximately 20 nm. The L_{MFP} decreases to approximately 10 nm for electrons with 2 eV energy in all four metals [25]. Typically, hot holes have longer L_{MFP} compared to hot electrons, favoring large transport probability and injection efficiency [26].

The simplest architecture to harvest plasmonic hot electrons is the metal-semiconductor (MS) Schottky junction. To facilitate the extraction of both electrons and holes, the metal nanoparticle is placed between the n-type semiconductor and p-type semiconductor, as shown in Figure 2.6. In this architecture, energetic electrons can be collected from the plasmonic metal nanoparticles provided they arrive at the interface with enough kinetic energy to overcome the existing barrier (Φ_B) [27].

2.2.2 Charge Injection

The Marcus theory describes the rate of electron transfer between two states. Later, this theory was further developed to evaluate the electron transfer from a single donating state to a continuum of accepting states such as the conduction band of a semiconductor [28] [29]. Electron transfer rate (k_{ET}) via the conduction band edge has been expressed by the so-called many-states Marcus formalism [30] [31]:

$$k_{ET} = \frac{2\pi}{\hbar} \int_{-\infty}^{+\infty} \rho(E) \langle H_{ab}(E) \rangle^2 \frac{1}{\sqrt{4\pi\lambda k_B T}} e^{-(\lambda+\Delta G)^2/4\lambda k_B T} \quad (2.16)$$

Here, ΔG refers to the Gibbs free energy variation with moving from the donating species to the accepting species, λ is the reorganizations energy, T is the temperature, $\rho(E)$ represents the density of unoccupied accepting states in the metal oxide semiconductor, $\langle H_{ab}(E) \rangle$ quantifies the physical overlap between initial and final states. In simple terms, the free energy change is the energy difference between the donating state and the bottom of the acceptor conduction band. The reorganizational energy includes all structural changes in the reactants and the environment during charge transfer. Generally, a plot of k_{ET} versus ΔG will show a steep rise when ΔG approximately equals λ , where the transfer dynamics depend on the recognition energy. After that, a gradual increase of the rate when ΔG is larger than λ , the regions are dominated by the density of electron-accepting states.

In general, there are two primary routes for hot electron transfer: indirect and direct pathways [32] [33]. In the indirect transfer mechanism [34], hot electrons are initially generated in the plasmonic metal nanoparticle. Subsequently, part of these hot electrons reach the interface and are transferred to the semiconductor. Due to the rapid relaxation via electron-electron scattering, only a very small fraction of plasmonic hot electrons with high potential energy, which are able to overcome the energy barrier at the interface, can be involved in the indirect transfer process [35]. The hot electron injection process competes with the electron-electron scattering process. This is one of the reasons that the indirect transfer process exhibits very low efficiency in practical experiments (typically <2%) [36] [37]. Another factor is that the back transfer of electrons may take place at the interface, particularly when the energy barrier height is low [38]. For the direct hot-electron transfer process [39] [40], the presence of suitable empty hybridized orbitals resulting from the strong interaction of the metal nanoparticle with the closely contacted semiconductors facilitates the direct generation of hot electrons in the empty hybridized orbitals during the dephasing of plasmon. Compared to the indirect electron transfer, the direct transfer process exhibits higher transfer efficiency and reduced energy loss. This is because the indirect transfer pathway suffers from a lot of energy loss in the electron-electron, and electron-phonon scatterings before the transfer occurs, as well as during the hot electron injection across the heterojunction interface. In contrast, the direct electron transfer pathway involves the direct generation of hot electrons in the hybridized orbitals owing to Landau damping, which avoids the electron-electron scattering in the metal and energy loss during the injection process across the interface. After injection, hot electrons will interact with the semiconductor and/or back transfer to the metal, which competes with the hot electron transfer processes, creating a barrier for the efficient utilization of plasmonic hot electrons.

3. Methods

This chapter provides information about the methodology that is used to conduct doctoral studies. In general, sample preparation, optical characterization, and device evaluation are included. Particularly, time-resolved spectroscopy has been broadly employed throughout this thesis to understand processes that occur from femtosecond to picosecond time scales.

3.1 Materials Preparation

3.1.1 Synthesis of the Au Nanoparticle

Bottom-up and top-down approaches are two strategies that have been classified to prepare metal nanoparticles. In order to form a clean nanomaterial film on the surface of the substrate with a large area, physical vapor deposition is very simple and materials could be deposited uniformly on substrates. As a top-down approach, thermal evaporation under high vacuum (10^{-5} torr) involves the generation of gas by heating metal beads placed on a resistive boat to the evaporation point, and condensation of gas molecules on the cold surface of the substrate. An in-situ quartz crystal microbalance monitors the thickness of the metal film. Ultrathin (less than 10 nm) evaporated gold films have well-defined island structures and optical properties similar to those of colloidal gold nanoparticles. This method was applied to get a 3 nm Au film on top of the TiO_2 layer. Upon further annealing of the Au film at 500°C , the height of Au structures increases, whereas their diameter decreases. As a result, the Au exhibits a quasispherical shape [41].

3.1.2 Preparation of Semiconductor Films

Spin coating has been widely employed in fabricating thin films for electronics. The advantages are rapid process, substrate tolerance, and inexpensive apparatus. Besides the composition of the ink, the film morphology could be adjusted by changing spin coating parameters such as speed and time. Four key steps can be used to simulate this approach. After depositing the solution on a static substrate (static method), rotary movement is started immediately. It usually takes few seconds to reach the required speed. In the beginning, most of the ink is flung away by the centrifugal force. Thus, the surface tension, viscosity, and rotation rate affect the film thickness. When the spreading

action stops, solvent evaporation controls the film formation. Due to the large amounts of ink used to cover the surface entirely in the first step, dropping the ink onto a rotating substrate (dynamic method) alternatively could reduce waste. In this thesis, SnO_2 and spiro-OMeTAD films were prepared by the static spin coating technique from the SnO_2 colloidal dispersion and spiro-OMeTAD solution respectively. The perovskite films were prepared using a two-step spin coating method. The PbBr_2 precursor solution was spin-coated firstly on the substrate by the static method, and the FABr solution was spin-coated on top of the PbBr_2 film by the dynamic method. The compact layer in a solar cell has the function to extract the photogenerated charges and prevent direct contact between the absorbing layer and the fluorine-doped tin oxide (FTO) electrode. Spray pyrolysis was chosen to prepare the compact TiO_2 layer with few pinholes. A thin film is formed by spraying a precursor solution on a heated substrate, where a pyrolytic reaction takes place to form the final chemical compound. Compact TiO_2 film was fabricated by spraying the solution containing titanium diisopropoxide bis(acetylacetonate), acetylacetonate, and ethanol as the solvent. After thermal annealing at 500°C , TiO_2 film shows the anatase crystal structure.

3.2 Scanning Electron Microscope (SEM)

To characterize the size and distribution of nanoparticles, the SEM technique is capable of producing images of the sample. The SEM is a microscope that uses electrons instead of light to form an image. When the electron beam is focused on the sample, interactions take place between the electron beam and atoms on the sample surface. Secondary electrons, backscattered electrons, and X-rays are ejected from the sample which are collected by detectors. The image is obtained by collecting the secondary electrons and backscattered electrons. SEM images were taken by using the Zeiss LEO1550 microscope (EHT = 3.00 kV). The morphology image indicates the shape and size of the Au nanoparticles. Since the backscattered electrons are sensitive to atomic number, the material contrast for the cross-section sample (FTO glass/ TiO_2 /Au/spiro-OMeTAD) could illustrate the composition difference. Therefore, the thickness of each layer was obtained.

3.3 Optical Characterization

3.3.1 UV-vis Spectrophotometer

The simplest and most direct method for informing the band structure of semiconductors is to measure the absorption spectrum. Furthermore, we can discover how the material absorbs in regions of the solar spectrum. As regards metal nanoparticles, the position of the localized surface plasmon (LSP) could

be measured which provides information on the size and concentration of nanoparticles.

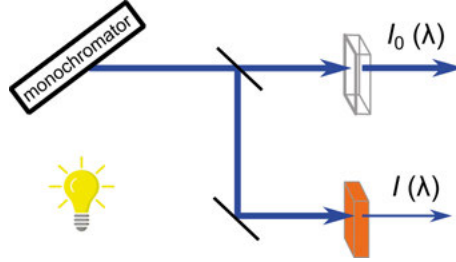


Figure 3.1. Simple schematic of the spectrophotometer.

Absorbance spectrum of a compound either in solution or film states is obtained by the ultraviolet-visible (UV-vis) spectrophotometer. In this thesis, the Cary 5000 instrument was used for absorption measurements. Its optical system (Figure 3.1) mainly has a light bulb, a monochromator, a beam splitter, and a series of optical mirrors to direct two light beams to the reference and sample ports respectively. The photomultiplier tube (PMT) detectors analyze the intensities of the transmitted light in the UV-vis region.

The absorbance behavior results in the attenuation of light passing through the material. The Beer-Lambert Law describes the relation of incident light (I_0) to transmitted light (I) by the following equation:

$$A(\lambda) = \log_{10} \frac{I_0(\lambda)}{I(\lambda)} = \varepsilon(\lambda)lc \quad (3.1)$$

At a certain wavelength (λ), A is absorbance, ε is the molar extinction coefficient of the compound in solution ($M^{-1}cm^{-1}$), l is the path length of the cuvette, and c is the solution concentration (M). As for thin film samples, the absorbance becomes:

$$A_\lambda = \alpha(\lambda)l \quad (3.2)$$

where α is the energy-dependent absorption coefficient (cm^{-1}) and l is the film thickness (cm). From the fundamental absorption (valence band-to-conduction band transition), we could calculate the energy gap of the semiconductor by the Tauc method which is based on the absorption coefficient expression (Equation (2.2)). The generalized equation is:

$$(\alpha h\nu)^{1/\gamma} = B(h\nu - E_g) \quad (3.3)$$

where B is a constant, and the γ factor is equal to 1/2 or 2 for the direct and indirect band gaps respectively. In practice, the linear fit of the fundamental peak is applied. Additionally, a linear fit used as a baseline is applied for the slope below the fundamental absorption. Therefore, an intersection of the two fitting lines gives the band gap energy estimation [42].

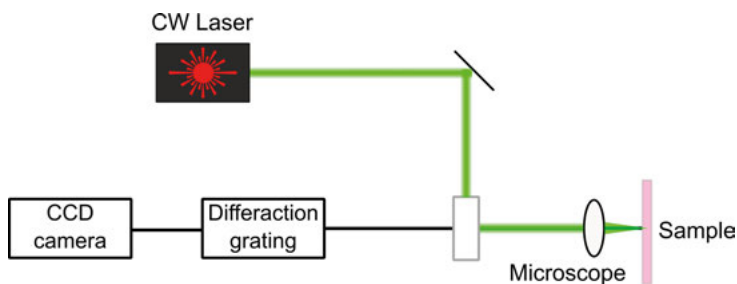


Figure 3.2. Schematic of the Raman spectrometer.

In solid-state solar cell research, film absorption is measured to study the optical properties of FAPbBr₃ perovskite and Au nanoparticles.

3.3.2 Raman Spectroscopy

Raman spectroscopy can be used to analyze the chemical composition of samples according to the vibrational modes of chemical bonds. The spectroscopic Raman effect is based on inelastic light scattering at the chemical bonds of a sample. The possibility to detect the Raman scattering is very low, typically less than one in a million excitation photons give rise to a single Raman event. Raman scattering can be further differentiated as stokes and anti-stokes scattering. Those bands at higher wavenumbers (blue shifted) are called anti-stokes Raman shifts and those at lower wavenumbers (red shifted) are called stokes Raman shifts. Normally, the intensities of the stokes-shifted Raman shifts are more intense and therefore used for qualitative and quantitative analysis. Elastic scattering at the same energy as the incident radiation is called Rayleigh scattering which has no information about the material. Raman spectroscopy provides qualitative and quantitative information. The compound distribution can be derived from the Raman spectrum by analyzing its specific chemical bonds.

Raman spectroscopy measurements were carried out on a Renishaw Reflex Raman microscope. As shown in Figure 3.2, it consists of a microscope through which the laser light strikes on the sample and the scattered light are collected. After the filtration of all the light except for the tiny fraction assigned to the Raman scattered light, a diffraction grating for separation of the Raman scattered spectral lines, and a charged-coupled device (CCD) camera are employed for the detection of the Raman spectrum. The excitation wavelength was at 532 nm and a 50 \times objective was employed during the measurement. With a single crystal Si reference, the system was calibrated with a reference line of 520.5 cm^{-1} . Raman spectroscopy illustrates the Raman shift of the spiro⁺ species. We use it to figure out the dependence of oxidation degree on the concentration of dopant in spiro-OMeTAD films.

3.3.3 Photoluminescence (PL) Spectroscopy

Photoluminescence spectroscopy is an important tool for the investigation of recombination processes in semiconductor materials. Following the promotion to conduction bands, electrons rapidly lose excess energy with the emission of phonons, and fall to the bottom of conduction bands. Eventually, various recombinations take place, such as radiative recombination via band-to-band transition and non-radiative recombination via bulk defects, surface dangling bonds, or Auger recombination.

Steady-state PL spectroscopy measures photoluminescence intensity as a function of wavelength at a time when the equilibrium between generation and recombination reaches. The spectra were acquired on the FS5 spectrometer (Edinburgh Instruments). Excitation light at a certain wavelength was generated from a xenon arc lamp.

Streak Camera

Time-resolved PL spectroscopy can be used to study fast radiation processes occurring over a very short time scale (from picoseconds to nanoseconds). The streak camera has the advantage of measuring the light intensity on both the time and wavelength axis. In addition, the temporal resolution could reach in the picosecond range.

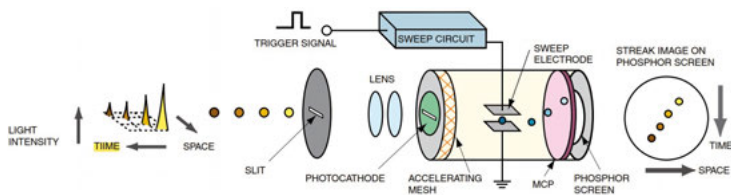


Figure 3.3. Principle of the streak camera [43]. Copyright 2008 by Hamamatsu Photonics K.K. Reprinted with permission.

Figure 3.3 shows the operating principle of the streak camera. The light pulse (e.g. fluorescence) to be measured is focused onto the photocathode of the streak tube through the slit, where the photons are converted into a number of electrons proportional to the intensity of the incident light. These electrons are accelerated and conducted towards the phosphor screen, and a high-speed voltage that is synchronized to the incident light is applied. The electrons are swept at high speed from top to bottom, after which they are bombarded against the phosphor screen of the streak tube and converted to an optical image. This 2D image contains both time and energy information about the fluorescence signal. If the light intensity of the streak image is very weak, an extra image intensifier could be inserted to amplify the low light-level streak image. During the measurement of the transient emission spectroscopy, the pump light was generated from the fundamental 1030 nm laser (<300 fs, 200 kHz). A streak camera (C5680 Blanking unit, M5675 Syn-

chroscan Sweep Unit, Hamamatsu) equipped with a charge-coupled device (CCD) camera (C4742-95, Hamamatsu) was employed to collect the diffracted emission. The time window is 2 ns and the instrument response function (IRF) is about 25 ps.

In this thesis, a combination of steady-state and time-resolved PL spectroscopy helps to understand the charge transfer at n-type semiconductor/FAPbBr₃ interfaces. Also, the effect of excitation density on the quantities of excited species and their kinetics were measured.

3.3.4 Femtosecond Transient Absorption Spectroscopy

Photophysical phenomena, such as the generation of excited charge carriers, relaxation, recombination, and transfer processes, usually occur between fs and ps. To monitor the kinetics of those ultrafast processes, femtosecond transient absorption spectroscopy was employed. In transient absorption spectroscopy, a monochromatic pulse, referring to the pump, strikes the surface of the solid film with the electrons in the excited states. Then, a weak probe pulse will pass through the same sample position after a certain delay time with respect to the pump pulse. Hereafter, both the transmitted probe pulse intensities with and without pump pulse are recorded. Thus, changes in the absorption spectrum could be calculated according to the equation:

$$\Delta A(\lambda, t) = A_{\text{pump}}(\lambda, t) - A_{\text{no pump}}(\lambda, t) \quad (3.4)$$

By varying the time delay, a spectrum containing the information on the relationship of the ΔA with time t and wavelength λ will be obtained. In general, several signals representing different processes could be distinguished during the data analysis. The ground state bleaching (GSB) band is a negative signal in the ΔA spectrum because of the depopulation of electrons in the ground states. In accordance with equation 3.4, $A_{\text{pump}}(\lambda, t)$ is smaller than $A_{\text{no pump}}(\lambda, t)$ and $\Delta A(\lambda, t)$ is negative. Secondly, stimulated emission (SE) comes from the relaxation of the excited states to the ground states with the assistance of the pump pulse. Since the transmitted light intensity increases by adding the stimulated emission, $A_{\text{pump}}(\lambda, t)$ is smaller than $A_{\text{no pump}}(\lambda, t)$ and $\Delta A(\lambda, t)$ is negative, and a negative signal appears in the ΔA spectrum as well. The third transient signal is attributed to the excited states absorption and a positive signal in the ΔA spectrum appears.

Transient absorption spectroscopy was carried out on a femtosecond transient absorption spectrometer (Figure 3.4). The laser system is a Ti:sapphire laser system with a repetition rate of 3 kHz and a pulse duration of 40 fs. After splitting the fundamental beam, both pump and probe pulses are generated from two separate optical parametric amplifications (OPA). In transient infrared absorption spectroscopy (TIRAS), the pump pulse passes through a delay stage, and the probe pulse is the broadband infrared light. The instrument response function is ca. 100-200 fs. For probing in the visible region,

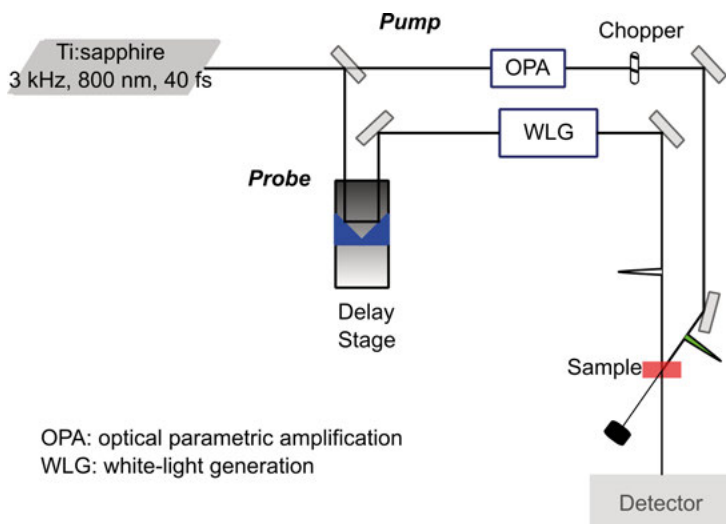


Figure 3.4. Schematic of UV-vis femtosecond transient absorption setup.

the probe pulse passes through a delay stage and the white light is produced from a CaF_2 optical window.

By analyzing the femtosecond transient absorption spectroscopy, electron-phonon relaxation time was studied on the plasmonic Au film. What's more, the injection of free charge carriers into the semiconductor material was observed, and the kinetics were obtained by fitting the decay curves.

3.4 Device Characterization of Solar Cells

3.4.1 Current-Voltage (I-V) Measurement

To acquire the solar energy conversion efficiency of the solar cell, important parameters including voltage, electric current, and maximum output power, can be experimentally measured by the current-voltage (I-V) measurement under light illumination. I-V measurement is done by measuring the current flowing through the device while varying the bias voltage. A commercial source measure unit (SMU) from Ossila is capable of simultaneously supplying voltage and measuring current with very high accuracy. Sometimes, the applied bias voltage can alter the electronic properties of a device. This can lead the current to change over time, even when the voltage is kept constant. Hence, we need a pause (voltage settle time) between setting a voltage and measuring the current. The illumination source is a light-emitting diode (LED) solar simulator, which can replicate various light spectra such as the air mass 1.5 global (AM 1.5G) spectra. An example of the I-V curve is presented in Figure 3.5.

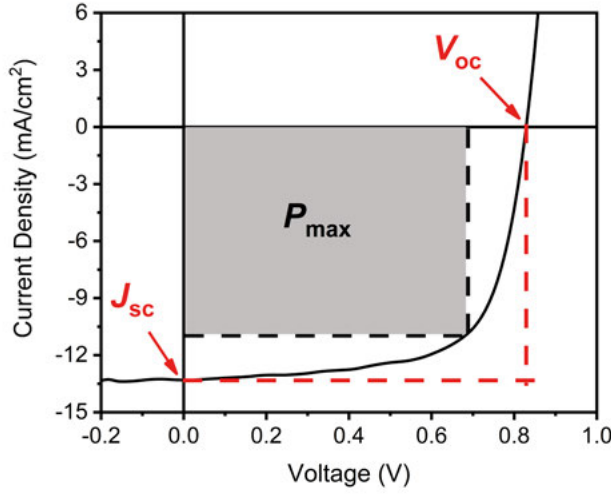


Figure 3.5. I-V characteristics of a solar cell under AM 1.5G spectrum.

The power conversion efficiency (PCE) of a solar cell is the ratio of the maximum power (P_{\max}) to the incident light power (P_{in}), see equation 3.5. Here V_{oc} is the open-circuit voltage; J_{sc} is the short-circuit current; and FF , an abbreviation for fill factor, is expressed as equation 3.6.

$$PCE = \frac{P_{\max}}{P_{\text{in}}} = \frac{V_{\text{oc}} J_{\text{sc}} FF}{P_{\text{in}}} \quad (3.5)$$

$$FF = \frac{P_{\max}}{V_{\text{oc}} J_{\text{sc}}} = \frac{V_m J_m}{V_{\text{oc}} J_{\text{sc}}} \quad (3.6)$$

From the I-V measurements, the effect of the transport layer conductivity on the performance of solar cells has been illustrated.

3.4.2 Quantum Efficiency

In I-V measurements, less information on spectral response and quantum efficiency is provided. To know the charge collection and loss as a function of wavelength, incident photon-to-electron conversion efficiency (IPCE) should be measured. IPCE is a quantity whose value characterizes the quantum efficiency that photons at each wavelength harvested by the solar cell. It is defined as the ratio of collected carriers to the number of incident photons at each wavelength:

$$IPCE(\lambda) = \frac{\text{number of electrons output}(\lambda)}{\text{number of incident photons}(\lambda)} \quad (3.7)$$

A xenon lamp coupled to a monochromator in the measurement setup is used to generate a near-monochromatic beam. A standard silicon photodiode is used as the reference to validate the IPCE system. The J_{sc} of the solar cell can also be calculated by the integration of IPCE and spectral irradiance. In most cases, this value should be consistent with the J_{sc} obtained from the I-V measurement.

Ideally, the IPCE value should be 100%. However, solar cells always suffer from different kinds of energy losses, such as absorption loss and recombination loss in reality. Therefore, absorbed photon to current conversion efficiency (APCE) provides further insight into the properties of the solar cell. APCE is calculated by dividing the IPCE value by the absorptance. Absorptance is a term that describes the ratio of the absorbed to the incident radiant power light. When taking the absorptance into consideration, we could obtain the APCE value which shows how efficiently the numbers of absorbed photons are converted into current.

The quantum efficiency measurements of the plasmonic solar cell verify the excitation of LSPR and the following extraction of free electrons and tell us the energy losses as well.

3.5 Conductivity

To test the transport properties of the transport layers in the solar cell, conductivity is needed. Under the dark condition, direct current (DC) conductivity measurements were conducted to study the electrical property. Ohmic contacts on both sides of the semiconductor film were made with silver electrodes and FTO glass respectively. The silver electrode, with a thickness of 100 nm, was evaporated in a vacuum on top of semiconductor layers. From the linear and symmetric I-V curve, the conductivity σ is determined from its slope according to the equation below[44],

$$I = \sigma \frac{A}{d} V \quad (3.8)$$

where d is the sample thickness and A represents the area of the silver electrode. TiO_2 and SnO_2 films present different conductivity properties under the measurement.

4. Electron Transport Layer/FAPbBr₃ Interface in the Perovskite Solar Cell (Paper I and II)

Currently, the remarkable advancement in power conversion efficiency (PCE) achieved in lead halide perovskite solar cells presents a highly promising alternative to silicon solar cells. In addition, perovskite materials would also be cheap to produce and easily deposited onto most surfaces including flexible and plastic ones [45] [46]. The general chemical formula for perovskite is ABX₃. A and B represent two different cations while X denotes an anion.

In this chapter, a bromide-based perovskite (FAPbBr₃) with a direct bandgap of 2.2 eV is used for studies because of the high open-circuit voltage (V_{oc} , up to 1.639 V) for planar solar cells [47] [48]. The crystal structure is shown in Figure 4.1a. The A site is formamidinium (FA), the B site is Pb and the X site is Br. Figure 4.1b illustrates the main photophysical processes in perovskite solar cells [49]. Following the absorption of photons by the perovskite layer, the generation of excitons or carriers occurs within the femtosecond to picosecond time range [50]. These charge carriers then traverse the active perovskite absorber layer, which typically requires a few nanoseconds. Subsequently, the extracted charge is collected by the charge transfer layer, a process that typically takes a few microseconds [51]. Finally, the carriers are transported through an external circuit, delivering power to the connected load. Throughout these processes, there is a loss of a certain percentage of charge carriers due to bulk and interface recombination [52]. A straightforward but versatile tool to understand recombination is photoluminescence (PL) spectroscopy [53].

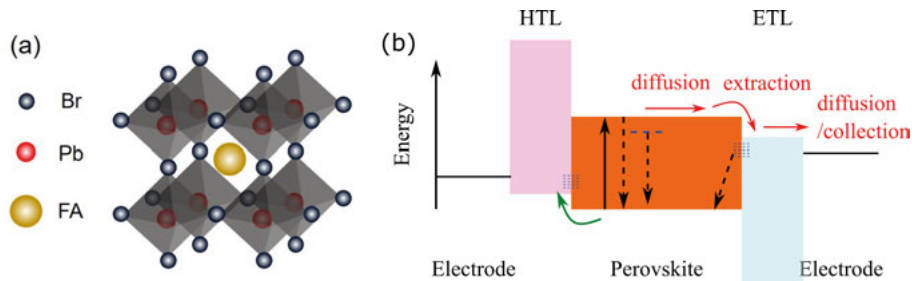


Figure 4.1. (a) Crystal structure of FAPbBr₃ perovskite. (b) Schematic diagram of the photophysical processes in perovskite solar cells. Blue dashed lines represent the bulk and interface defects. The black solid arrow represents the generation of charge carriers. The dashed arrows represent the recombination.

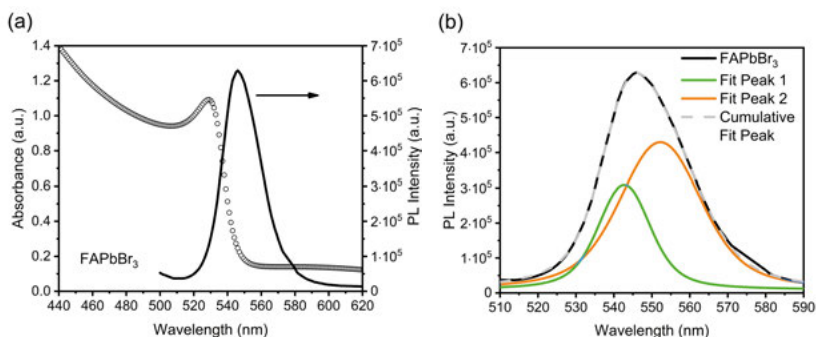


Figure 4.2. Steady-state UV-vis absorbance and emission upon excitation at 470 nm of FAPbBr₃. (a) Overlapped signal of absorbance and emission and (b) deconvolution of the emission signal.

By using transient energy-resolved photoluminescence measurements herein, the excited states (excitons and free carriers) and PL properties of the FAPbBr₃ material were investigated. Then, interfacial charge transfer indicated by PL quenching demonstrated differences between SnO₂ and TiO₂ semiconductors. Finally, modification of the interface by adding the KI into SnO₂ suggested the altered charge extraction process.

4.1 Photoluminescence of the FAPbBr₃ Film

Figure 4.2a shows the UV-vis absorbance and PL of the perovskite film on the cover glass substrate. The absorption edge wavelength is around 545 nm and a distinct excitonic peak is situated at approximately 529 nm [54]. The photoluminescence spectrum exhibits an overlap with the absorption edge and features its peak at 546 nm. The deconvolution of the PL peak results in two components (Figure 4.2b). The presence of the doublet could be related to different phases existing in the material, defect-trapping states, or emissions from the free carriers and the excitons [55] [56] [57]. Phase transition in the perovskite crystal structure takes place upon varying the temperature. Specifically, FAPbBr₃ possesses high phase stability, and its film crystallizes into a cubic structure at room temperature [58]. According to the X-ray diffraction pattern depicted in Figure S5 in the supporting information of paper I, the cubic phase was observed in the FAPbBr₃ film, consistent with previously published results [59] showing major planes such as (100) at 14.76° and (200) at 29.74°. Therefore, the possibility of a mixture of crystalline phases is ruled out. Regarding the overlapping characteristics of absorbance and emission spectra and the relatively narrow PL peak, emissions correlated to traps are not possible. The thickness of the perovskite thin film was about 300 nm. Therefore, the self-absorption effect could also be excluded which has been

attributed to the double peaks PL spectra in perovskite single crystals (thickness of 1 mm) [60].

A more plausible interpretation is that the emissions are associated with the recombination of free carriers (resulting in the higher energy PL peak) and excitons (resulting in the lower energy PL peak). The exciton binding energy was approximately 60 meV, estimated from the energy difference between those two peaks. This value is much larger than the thermal energy at room temperature (26 meV). Previous studies have reported different exciton binding energies for perovskites ranging from 20 meV up to 80 meV by various techniques [61] [62]. And the tri-bromide perovskite has notably higher exciton binding energy than the tri-iodide perovskite counterpart [63].

The lifetime of photoexcited species in FAPbBr₃ was extremely long (about 200 ns) obtained from the PL decay via time-correlated single-photon counting (TCSPC) method [45]. To investigate the above hypothesis, I conducted a time- and energy-resolved photoluminescence (TER-PL) study using a streak camera and a femtosecond laser pulse excitation (Figure 4.3a). The excitation wavelength was at 515 nm, exceeding the band gap energy of the perovskite, and the laser pulse duration was approximately 300 fs. In such conditions, the early-time (ps timescale) charge carrier dynamics were studied, which is not feasible to observe by methods like TCSPC. During these early times, excitons and free carriers coexist. In principle, distinct rising components for each species in transient PL spectra should be observed, as well as varying exponential decay behaviors.

The kinetic trace of the lower-energy component was selected within the 565-575 nm range. This trace exhibited a rapid rise of 37 ps and a single exponential decay with a time constant (τ) of 520 ± 12 ps, as depicted in Figure 4.3b. The rising time referring to the formation of charges is close to the instrument response function (IRF) (ca. 25 ps). Lifetimes in tens to hundreds of picoseconds suggest that multiple excitons are being formed since single excitons have lifetimes in tens of nanoseconds [64]. A longer lifetime results in a longer diffusion length in perovskites, beneficial for superior solar cell performance [65] [66] [67]. The decay behavior follows the recombination of excitons. As for the high-energy component, data were analyzed between 520 nm and 530 nm. The kinetic trace was fitted with a bi-exponential decay, namely $\tau_1 = 120 \pm 11$ ps (50%) and $\tau_2 = 1222 \pm 69$ ps (50%) (Figure 4.3c). The rising time (55 ps) is more significant than the IRF (ca. 25 ps) and longer than the rising of excitons, suggesting that the excited charge carrier has reached its maximum concentration before the decay. Therefore, the rising time is associated with the cooling down of charges and filling the emissive state. More detailed information can be found in Supporting Information Table S2 of paper I.

After distinguishing the free carriers and excitons through the deconvolution of the PL spectrum, I studied the fraction of free charges under various laser fluences. Considering the perovskite film absorbance and thickness, the

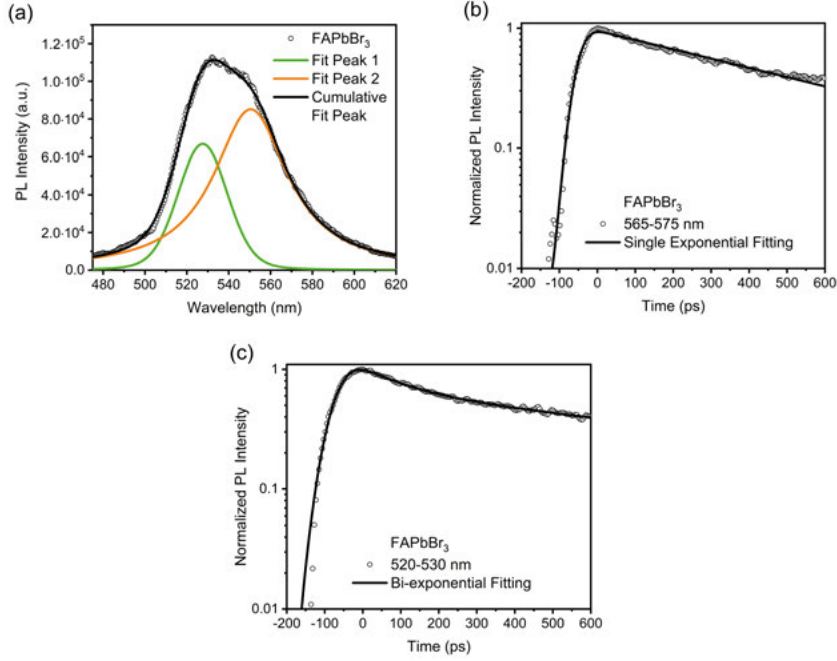


Figure 4.3. TRPL of FAPbBr₃ on glass upon excitation at 515 nm with a 300 fs laser pulse and a photon energy of 18 W/cm². (a) Deconvolution of the accumulated PL signal after 1000 ps; (b) kinetic decay of the signal extracted between 565 and 575 nm (bounded excitons); and (c) kinetic decay of the signal extracted between 520 and 530 nm (free carriers). Note that TRPL fittings are shown to 600 ps but performed over a 1 ns time range, ensuring at least 60-70% signal decay.

laser fluence can be converted to the excitation density within the FAPbBr₃ film. As mentioned in subsection 2.1.1, the Saha-Langmuir equation (Equation 2.6) describes the equilibrium established between excitons and free carriers. In Figure 4.4a, the free charges fraction x in response to changes in excitation density n at room temperature is controlled by adjusting the binding energies, following the Saha equation.

Taking into account that the exciton binding energy is about 60 meV and assuming a reduced exciton mass (μ) equal to 0.15 m_e [68], I converted the particle fractions into their density in the film as a function of excitation density. The simulated results are shown as the solid lines in Figure 4.4b. Five experimental points under different laser fluences were obtained by deconvolution and integrating the respective PL peaks when PL intensity reached the maximum. As illustrated in Figure 4.4b, the agreement between simulated and experimental data also supports the measured value of exciton binding energy. It is worth noting that the carrier density was below the Mott density

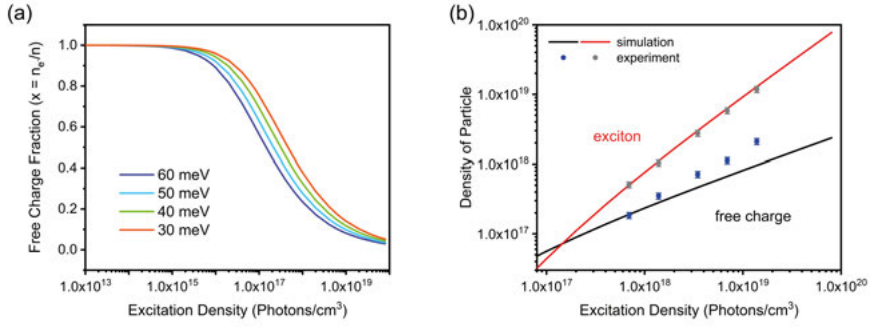


Figure 4.4. The population of excited species in the FAPbBr₃ film under various excitation densities. (a) Simulation of the free charge according to the Saha-Langmuir equation with a binding energy E_B of 60 meV and a reduced mass of exciton μ of 0.15 m_e . (b) Simulation data calculated by multiplying the species fraction with the excitation density and experimental data of the exciton and free charge densities calculated from PL^{\max} .

(around 10^{20} cm^{-3}) to avoid the exciton-exciton interaction and dissociation into electron-hole plasma [68] [69] [70].

4.2 TiO₂ vs SnO₂

When photoexcited charge carriers in the absorber layer are transferred to the electron transport layer (ETL), the intensity of the radiative recombination will be decreased referring to the quenching effect [71]. Thus, the TER-PL measurement could be employed to investigate such change and provide information on the charge transfer process. FAPbBr₃ has high photoluminescence quantum efficiency and is sensitive to the PL quenching measurement [72] [73]. Two common semiconductors (TiO₂ and SnO₂) as the compact electron transport layer were selected for the following studies.

Figure 4.5a-c shows the different PL quenching effectiveness between SnO₂ and TiO₂ under various laser fluencies. The integrated PL spectra, observed after 1000 ps, reveal that TiO₂ exhibits a notably higher quenching efficiency, especially at lower fluence levels. The ratio of unquenched PL emissions from the perovskite material against the excitation density is presented in Figure 4.5d. As the laser fluency increases, the disparities in quenching efficiencies between the two materials tend to diminish, suggesting a degree of saturation.

Since the initial 1000 ps of the PL decay reflects the charge transfer process from the perovskite to the ETL, the above results indicate that TiO₂ is better than SnO₂ for electron injection. Previously, injection efficiency was evaluated by measuring the terahertz conductivity in the nanoporous metal oxide films after photoexcitation of the attached Z907 ruthenium dye [74]. TiO₂ shows the highest value than SnO₂ and ZnO. A direct correspondence between the

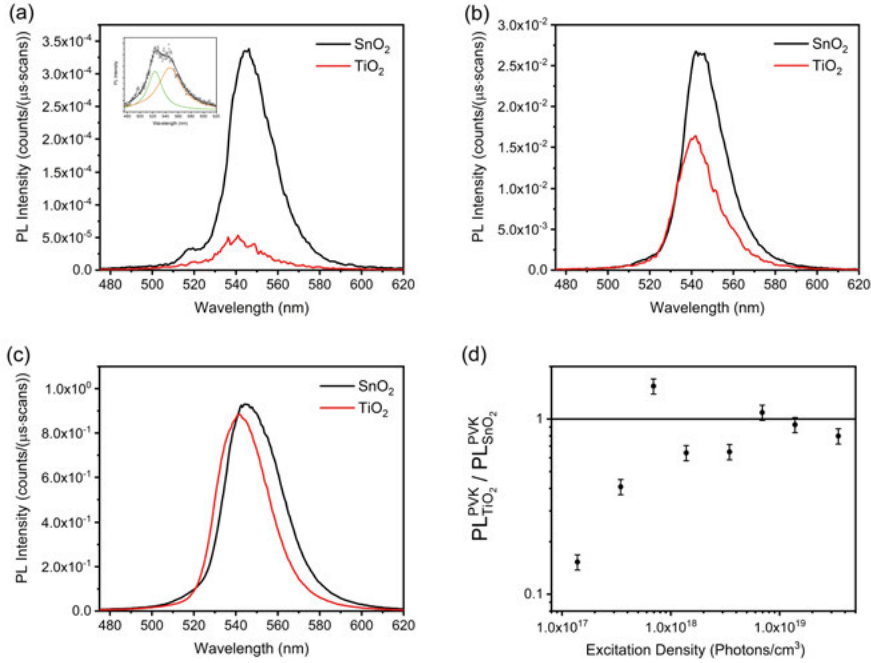


Figure 4.5. The integrated TER-PL spectra (1000 ps) of the FAPbBr₃/ETL films under various excitation densities were normalised by the exposure time and the scan number. (a) $\sim 1.4 \times 10^{17}$ photons per cm^3 , (b) $\sim 1.4 \times 10^{18}$ photons per cm^3 , and (c) $\sim 1.4 \times 10^{19}$ photons per cm^3 . Inset figure (a) shows the deconvolution of the integrated TER-PL spectra (1000 ps) of the FAPbBr₃ films under an excitation density of 1.4×10^{17} photons per cm^3 . (d) The ratio of PL intensity from the unquenched perovskite layer as a function of laser fluencies. PVK is the abbreviation for perovskite

performances of dye-sensitized solar cells (DSSCs) and the electron injection efficiency is obtainable and the electron injection rate is readily determined. However, perovskite solar cells with the SnO₂ ETL have demonstrated higher efficiencies [75] [76] [77] than other semiconductors, due to better band alignment at the interface and higher conductivity.

The rate of electron transfer from the electron donor to the electron acceptor is driven by their energy difference, described by the Marcus model [78]. This energy difference is quantified by the Gibbs free energy (ΔG) of the reaction. Several significant factors, including the electronic coupling between the donor and acceptor, solvent reorganization, and the energy difference between the donor and the acceptor affect the transfer rate. Considering the parameter of the conduction band offset, the conduction band edge of SnO₂ lies 0.2-0.3 eV below that of TiO₂ [79]. Hence, these two systems have similar values of the energy difference as the driving force. Thus, the explanation for the higher transfer rate must be sought in the electronic coupling between the donor and

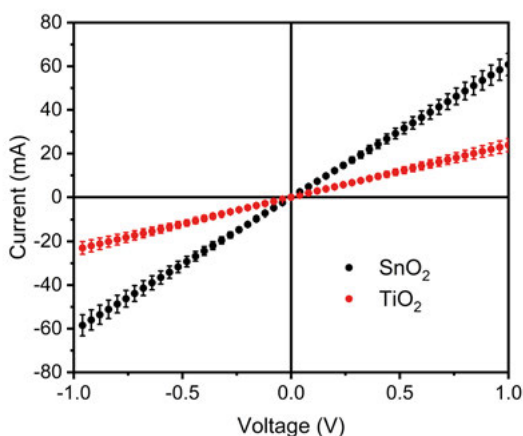


Figure 4.6. Dark I-V curves for samples with the structure of FTO/ETL/Ag (100 nm).

acceptor and the density of states (DOS) expressed in the Marcus-Gerischer model [80]. Systems with higher DOS are expected to exhibit higher electron transfer rates. Theoretical calculations have indeed demonstrated that these two n-type semiconductors possess distinct band-edge structures, with TiO₂ featuring a higher DOS from the outset of the conduction band edge [81]. This attributes the higher quenching rate observed for TiO₂ compared to SnO₂.

The charge transport layer is not only required for efficient charge injection. The higher conductivity facilitates the charge transport and prevents interfacial recombination. Similar findings have been reported in other systems, such as plasmonic-semiconductor interfaces [82]. SnO₂ shows steeper slope in the I-V curve (Figure 4.6), indicates higher conductivity than TiO₂. Solar cell efficiency is generally affected or even controlled by several factors, including carrier transfer and transport. When interfacial electron transfer is no longer rate-limiting, it becomes difficult to use the PL characterization to establish a correspondence between cell performance and electron transfer rate [83].

To assess the difference between TiO₂ and SnO₂ in terms of their ability to extract free carriers and bound excitons, the accumulated time-resolved PL spectra within 1000 ps were normalized (Figure 4.7). As the excitation density increases, the PL peaks tend to broaden in both systems, with the FAPbBr₃/SnO₂ system displaying even broader peaks. Also, the PL band edges undergo asymmetric shifts with increasing laser fluency. Consequently, the analysis of the normalized PL band edge shifts can provide information on the extent of carrier extraction and offers insights into whether free carriers exhibit higher selectivity compared to bound excitons.

When examining the lower energy region (associated with bound excitons), there is no substantial difference in their proportion between the two systems (Figure 4.8b). This suggests that exciton quenching, whether through direct

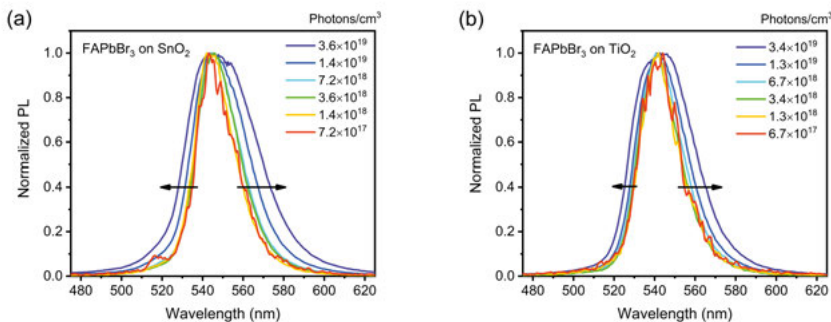


Figure 4.7. Normalized PL spectra of the FAPbBr₃/ETL films under various excitation densities: (a) FAPbBr₃/SnO₂ and (b) FAPbBr₃/TiO₂.

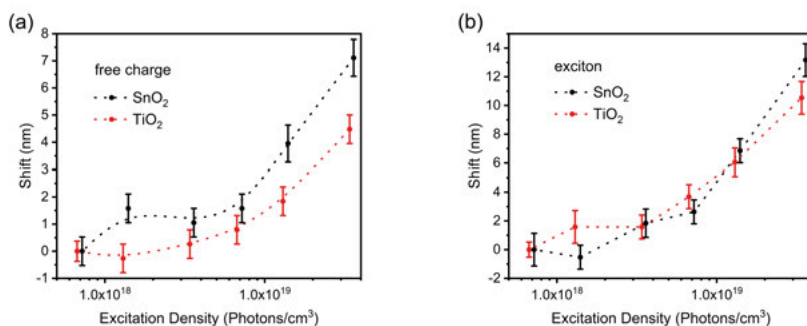


Figure 4.8. Edge shifts of the FAPbBr₃/ETL films at various excitation densities and the reference sample was measured under the lowest excitation density: (a) Left edge and (b) right edge.

processes or via their dissociation into free carriers, is relatively consistent in both systems. Therefore, it is unlikely to be the reason for the differences in quenching rates.

In contrast, the analysis of the higher energy region (involving free carriers) reveals that SnO₂ is less effective at quenching them, as indicated by a more significant band edge shift compared to TiO₂ (Figure 4.8a). This observation again aligns with the hypothesis that a higher density of states (DOS) facilitates enhanced overlap between the donor and acceptor, leading to higher transfer rates.

4.3 Modification of the SnO₂ ETL

The perovskite crystal structure is interrupted at the surface. Therefore, point defects (e.g., atomic vacancy defects) and higher dimensional defects (such as

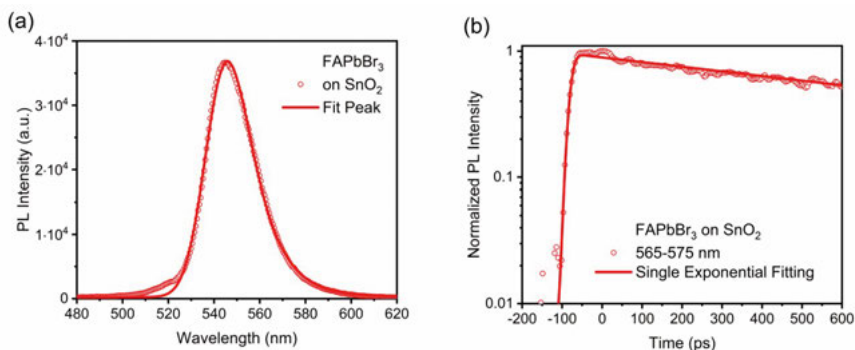


Figure 4.9. TRPL of FAPbBr₃ on SnO₂ upon excitation at 515 nm with a 300 fs laser pulse and a photon energy of 18 W/cm². (a) Deconvolution of the accumulated PL signal after 1000 ps and (b) kinetic decay of the signal extracted between 565 and 575 nm (bounded excitons). Note that TRPL fittings are shown till 600 ps but performed over a 1 ns time range, ensuring at least 60-70% signal decay.

grain boundaries) are generated at the interfaces between perovskite materials and the SnO₂ ETL.

There are many methods to tackle this issue, such as defect state passivation by potassium cation. Potassium halides are commonly inserted as the thin interlayer between SnO₂ and FAPbBr₃ [84] [85] [86]. K⁺ ion contributes to better crystallinity and morphology of perovskite films, suppressing the recombination at the interface and leading to longer bulk recombination [87]. What's more, the defect energy level is decreased together with a decrease in defect density [88]. Here, the KI was added in the SnO₂ colloid suspension [89], aiming to have extra effects such as the formation of the Sn-O-K bonding and modification of SnO₂ energy levels.

TRPL illustrates the accumulated PL signal after 1000 ps (Figure 4.9a). Notably, the best-fit analysis revealed that a rising edge and a single exponential decay (Figure 4.9b). Furthermore, this emission is located at around 555 nm, suggesting that the signal is related to bounded excitons. This discovery emphasizes a preference for electron extraction from the free-carrier population, as depicted in the Jablonski diagram in Figure 4.11a, resulting in the suppression of this emission pathway. Fitting of the emission could be done with a single exponential ($\tau = 1468 \pm 48$ ps) and a rising edge with 34 ps (Figure 4.9b), aligning consistently with bounded exciton emission. The ultrafast rising edge reaffirmed the creation of multiple excitons, as previously reported [64].

Figure 4.10 shows the fitting results of the TRPL after 1000 ps. The TRPL peak consists of two components (Figure 4.10a), similar to the deconvolution result of steady-state PL for the perovskite alone. However, the accumulated TRPL emission is different from the result obtained for the perovskite on bare SnO₂. Analysis of the kinetic traces revealed that the higher energy com-

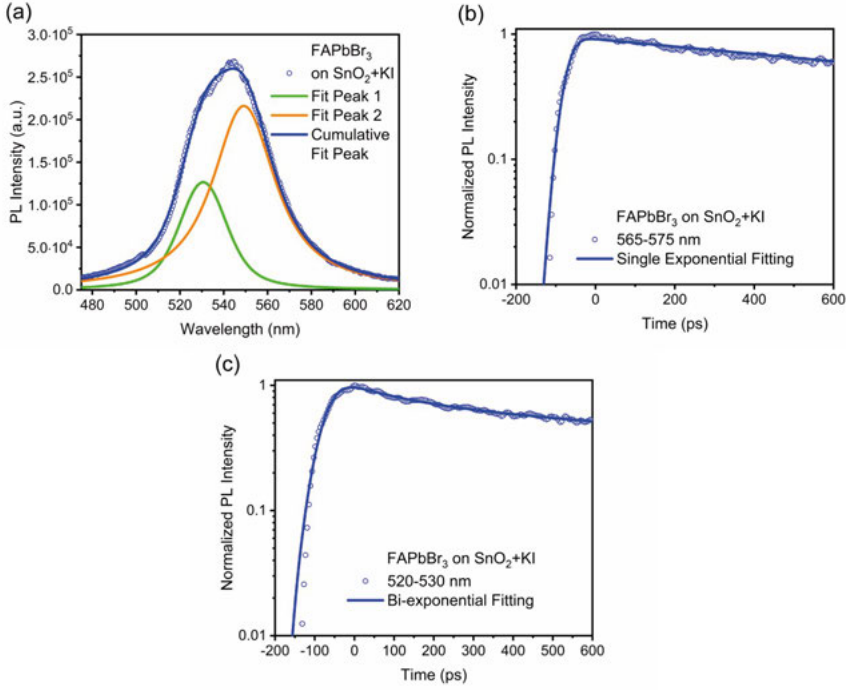


Figure 4.10. TRPL of FAPbBr₃ on SnO₂ treated with KI upon excitation at 515 nm with a 300 fs laser pulse and a photon energy of 18 W/cm². (a) Deconvolution of the accumulated PL signal after 1000 ps; (b) kinetic decay of the signal extracted between 565 and 575 nm (bounded excitons); and (c) kinetic decay of the signal extracted between 520 and 530 nm (free carriers). Note that TRPL fittings are shown till 600 ps but performed over a 1 ns time range, ensuring at least 60-70% signal decay.

ponent has a rising edge with about 48 ps. The intensity decay requires a bi-exponential model to be fitted with $\tau_1 = 123 \pm 19$ ps (38%) and $\tau_2 = 1883 \pm 140$ ps (62%) (Figure 4.10c). This refers to the free-carrier emission. The component at lower energy was fitted with a single exponential decay ($\tau = 1168 \pm 36$ ps) and a rising function of 16 ps that is shorter than our IRF (Figure 4.10 b). This part is related to the bounded exciton emission. Kim et al reported that the potassium treatment induces an upward shift of the conduction band maximum and Fermi energy of SnO₂ [90]. In order to reduce the interface recombination, Minemoto and Murata concluded from simulation results that the ideal position of the conduction band in the block layer is determined to be approximately 0.0 to 0.3 eV higher than the conduction band in the perovskite absorber with planar junction configuration [91]. Consequently, the significant change of the electron extraction ratio of the bounded excitons and the free electrons (Figure 4.11b) is due to the modification of the band alignment at the interface by the KI addition.

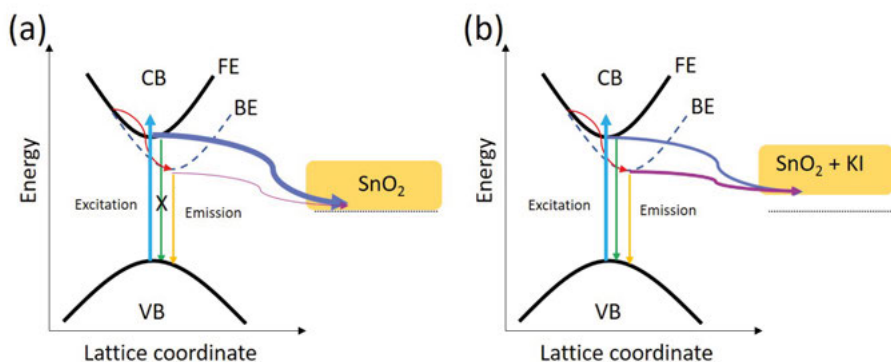


Figure 4.11. Jablonski-type diagrams summarizing photophysics of FAPbBr₃ on (a) SnO₂ and (b) KI-treated SnO₂. CB, conduction band; VB, valence band; FE, free electrons; and BE, bounded excitons.

4.4 Conclusion

In the two research studies featured in this chapter, photophysics of FAPbBr₃ and FAPbBr₃/ETL interfaces were presented. Time- and energy-resolved PL revealed the existence of two distinct emitting states in FAPbBr₃, linked to free carriers and bounded excitons. From the power-dependent transient photoluminescence measurements, two ETLs, SnO₂ and TiO₂, shown different photoluminescence quenching efficiencies. The electron transfer rate was unexpectedly higher for TiO₂, even though SnO₂ typically performs better as an electron transporting layer in solar cells. The result can be explained by the Marcus-Gerischer theory, which corresponds to the higher DOS of TiO₂. This enhances the overlap between the FAPbBr₃ and the electron acceptor (n-type semiconductor), thus promoting faster electron transfer. On the other hand, the superior conductivity of SnO₂ contributes to its proficiency in efficiently diffusing the injected charge. The findings indicate that photoluminescence (PL) alone does not serve as a reliable indicator of solar cell performance [92]. In contrast, the examination of PL peak asymmetric broadening proves to be a valuable approach for identifying the carriers being transferred and understanding how they evolve with changes in excitation fluency.

SnO₂ preferentially harvests electrons from the free-carrier population. The introduction of KI in the SnO₂ film modifies the electron extraction from excitons and free carriers.

5. Interfaces in the Direct Plasmonic Solar Cell (Paper III and IV)

Upon photoexcitation of the Au nanoparticle, the generated plasmonic hot electrons are injected into the TiO_2 conduction band. Based on the mechanism of plasmon-induced charge separation at the interface of Au- TiO_2 photoanode, the solar cell with Fe^{2+} electrolyte as the electron donor was reported in 2005 [93]. Since the absence of an energy gap in plasmonic nanoparticles, the open-circuit voltage (V_{oc}) depends on the potential of different electron donors, as well as the metal oxide semiconductor. In order to overcome some disadvantages of liquid electrolytes such as electrode corrosion and leakage, various organic (poly(N-vinyl carbazole) (PVK), N, N'-Bis(3-methylphenyl)-N, N'-diphenyl benzidine (TPD), 4,4'-bis[N-(1-naphthyl)-N-phenylamino]biphenyl (NPD)) and inorganic (CuI, CuSCN) solid-state materials have been exploited for the hole transport layer [94]. Wang et al. [95] reported the hot electron extraction in the plasmonic solar cell consisting of a metal-insulator-metal (MIM) structure. The current was produced as hot electrons were injected above the thin insulating barrier.

And with the development of the dye-sensitized solar cell, spiro-OMeTAD (2,2',7,7'-tetrakis[N,N-di(4-methoxyphenyl)amino]-9,9'-spirobifluorene) was used to fabricate solid-state direct plasmonic solar cells (DPSC) [96]. Considering the transparency and fabrication techniques, the device with scattered Au nanoparticles sandwiched between compact TiO_2 and thick spiro-OMeTAD layers was employed (Figure 5.1). This structure resembles the n-i-p type perovskite solar cell. The average size of Au nanoparticles is 15 nm.

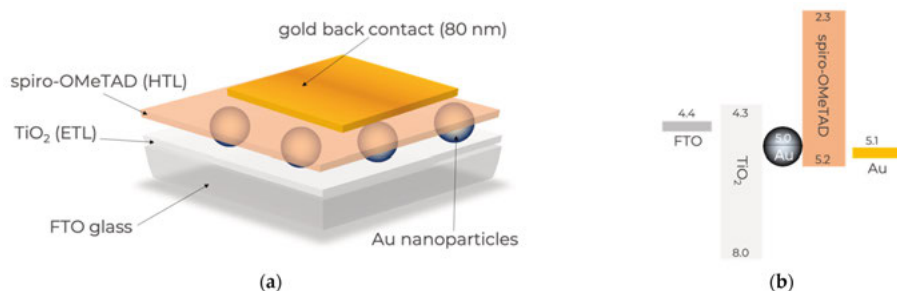


Figure 5.1. Schematic representation of n-i-p DPSC architecture. (a) Constituents of the DPSC used herein; (b) energy level diagram (in eV unit) of the main constituents according to what has been published elsewhere [97].

Generally, the addition of Li-TFSI (lithium bistrifluoromethanesulfonimide) dopant increases the conductivity and hole mobility in spiro-OMeTAD [98] [99]. In this section, I will discuss the effect of the dopant concentration on the oxidized content of spiro-OMeTAD and the solar cell performance. In addition to the hot electron generation, plasmonic nanoparticles can also give rise to the optical absorption enhancement of TiO_2 , which will be considered on paper IV.

5.1 Direct Plasmonic Solar Cell

A representative I-V curve of the plasmonic solar cell is shown in Figure 5.2a. The molar ratio of Li-TFSI is 20% relative to the spiro-OMeTAD. The device was illuminated under a solar simulator accompanied by a long pass filter that removes light below the wavelength of 560 nm. In this case, any other potential absorption from the transporting layers is eliminated. Hence, only the plasmon is excited and contributes to the photocurrent. The I-V curve displaces characteristic diode behavior without any hysteresis. According to this curve, the V_{oc} was 0.23 V, J_{sc} was $65 \mu\text{A}/\text{cm}^2$ and the FF was 31%, respectively. The V_{oc} value is rather close to the energy difference between the fermi level of Au and the valence band of spiro-OMeTAD (Figure 5.1b). Regarding the rough FTO surface and very thin TiO_2 layer (20-30 nm), hot electrons might injected via quantum mechanical tunneling through the barrier formed as the band bending at the TiO_2/Au junction.

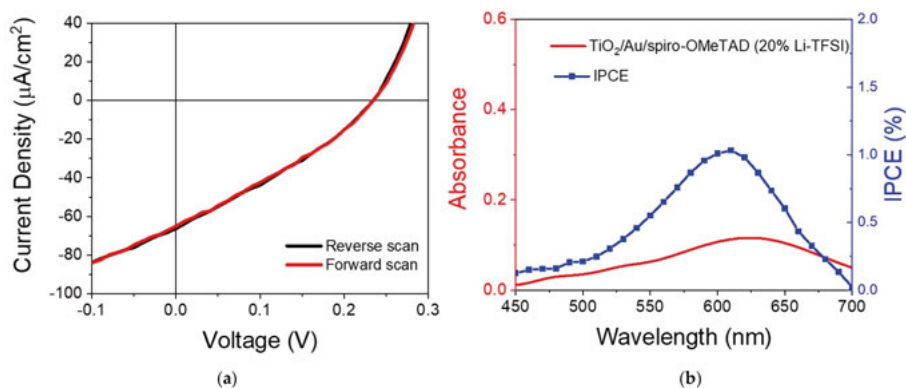


Figure 5.2. (a) I-V curve of the cell measured under simulated solar conditions with a cut-off filter that removes any light below 560 nm; (b) IPCE curve and optical absorbance of the cell.

Figure 5.2b shows that the incident photon-to-electron conversion efficiency (IPCE) curve followed the absorption profile of the Au LSPR band. This alignment provides confirmation that the solar cell parameters are related to charges

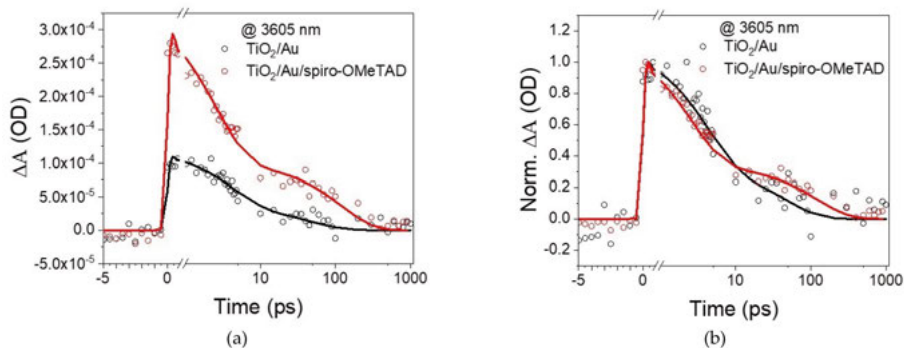


Figure 5.3. TIRAS measurements of charge injection for device containing spiro-OMeTAD with 20% Li-TFSI upon Au plasmon excitation at 550 nm. (a) Effect of the spiro-OMeTAD layer on the intensity of the transient data extracted at 3605 nm; (b) normalized intensity curves depicting the effect of the spiro-OMeTAD layer on the temporal evolution of the signal.

generated by Au plasmon excitation, rather than intra- or interband excitation. By utilizing the IPCE data, the absorbed photon-to-current conversion efficiency (APCE) could be extrapolated, yielding an approximate maximum value of 4.2%. This value aligns with what Reineck et al. measured for a solar cell containing Au particles of around 15 nm [100].

TIRAS measurements were executed to confirm the charge injection at the interfaces. Infrared absorption of free carriers results in broad and featureless positive absorption changes. As shown in Figure 5.3a, the kinetic trace extracted at 3605 nm offers insight into the temporal behaviour of the free carriers injected into the transporting layers after excitation at 550 nm. In the Au/TiO₂ system, a rapid increase in signal intensity suggests that electrons were injected into the TiO₂ layer. When the spiro-OMeTAD layer was spin-coated on top of the Au nanoparticle layer, a further increase in the intensity suggests that electrons and holes were injected. In section 2.2.2, charge injection via excited plasmons can take place directly (coherent injection) or indirectly via hot carriers. Currently, the transporting layers lack optical overlap with the Au plasmon, thus the direct injection is not favored. The prevailing mechanism is likely the hot carrier injection from the Au nanoparticles, which is anticipated to occur approximately 100 fs after plasmon excitation [21]. From Figure 5.3b, the rising edge component was not changed, suggesting that the hole injection is similar to the injection of hot electrons.

5.2 Dopant Concentration in Spiro-OMeTAD

By varying the Li-TFSI concentration, the hole-transporting properties of the spiro-OMeTAD layer will change with the quantity of spiro⁺TFSI⁻ species.

Table 5.1. Raman intensity analysis to quantify the abundance of oxidized spiro-OMeTAD.

Raman Peak	15% Li-TFSI	20% Li-TFSI	40% Li-TFSI	60% Li-TFSI
A (Intensity @ 730 cm^{-1})	1.19	1.04	1.05	1.74
B (Intensity @ 765 cm^{-1})	3.02	2.11	2.41	4.47
A/(A + B)	0.28	0.33	0.30	0.28

Figure 5.4a illustrates the Raman spectra of spiro-OMeTAD featuring different Li-TFSI molar concentrations. The overall spectral profile agreed with the previous report on the spiro-OMeTAD material, both in terms of peak position and relative intensity [101]. Analysis of peaks spanning the $600\text{--}900\text{ cm}^{-1}$ range was conducted to ascertain the degree of oxidized spiro-OMeTAD ($\text{spiro}^+\text{TFSI}^-$) within the samples (Figure 5.4b). Specifically, the peak at 731 cm^{-1} has been assigned to the C-S group within $\text{spiro}^+\text{TFSI}^-$ by Lamberti et al. [102]. Evaluating the relative amount of $\text{spiro}^+\text{TFSI}^-$ in the sample can be achieved by comparing its peak intensity against the Li-TFSI peak intensity at 760 cm^{-1} . Additionally, the peak near 710 cm^{-1} , attributed to tBP (4-tert-Butylpyridine), is observed.

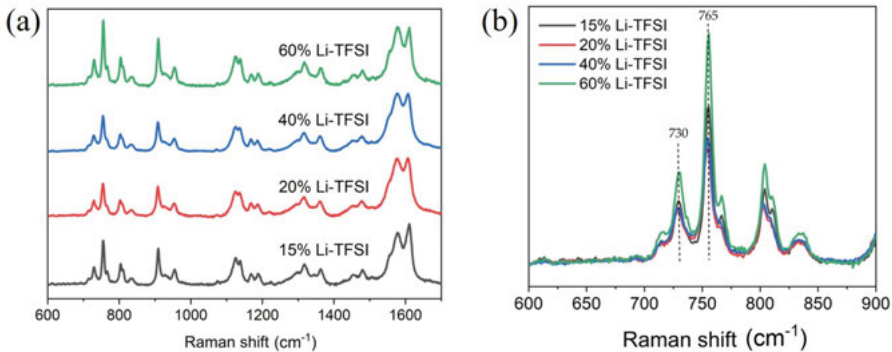


Figure 5.4. (a) Raman spectra of spiro-OMeTAD films with different Li-TFSI amounts. (b) Raman spectra of C-S group in the $\text{spiro}^+\text{TFSI}^-$ species and neutral spiro-OMeTAD with different Li-TFSI amounts.

Table 5.1 presents a comprehensive summary of the analysis. Notably, a substantial alignment emerges between the performance of the DPSC device (Figure 5.5) and the relative proportion of $\text{spiro}^+\text{TFSI}^-$. When 20% of Li-TFSI was added, the largest amount of $\text{spiro}^+\text{TFSI}^-$ species in the film provided the best solar cells. This infers the significance of considering the $\text{spiro}^+\text{TFSI}^-$ content when attempting to optimize solar cell performance.

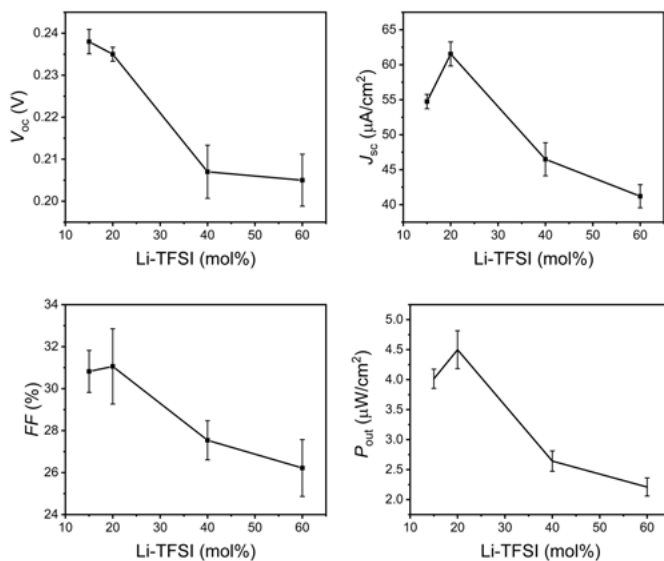


Figure 5.5. DPSC device performance as a function of Li-TFSI content spiro-OMeTAD under solar simulated illumination with a cut-off filter removing light below 560 nm. (a) Open-circuit voltage (V_{oc}); (b) short-circuit photocurrent (J_{sc}); (c) fill factor in percentage (FF); (d) power output ($P_{out} = V_{oc} \times J_{sc} \times FF$).

5.3 Absorption Enhancement

The enhanced electromagnetic fields and light-matter interaction in plasmonic structures could modulate the absorption in the semiconductor layer of solar cells. By light-trapping, the path length of a photon inside the semiconductor layer increases resulting in the enhancement of absorption probability. TiO_2 as an indirect band gap semiconductor normally has very low absorption coefficients, and the trap states as mentioned in subsection 2.1.1 also have low absorption coefficients. Approaches to enhance the absorption seem to be interesting and useful.

As shown in Figure 5.6a, the photoluminescence intensity became 20 times intenser when Au nanoparticle was adsorbed to the TiO_2 surface. At the lower temperature (77K), the intensity of the photoluminescence becomes more pronounced (panels d-g of Figure 5.6). Analysis of the kinetic traces extracted at 525 nm revealed that the ultrafast decay (<10 ps) is not affected by the presence of Au nanoparticles (Figure 5.6b). Power-dependent transient photoluminescence experiments exciting at 800 nm (Figure 5.6c) demonstrated a cubic dependence of the signal, suggesting the involvement of three photons in the upconversion process. This process is illustrated in Figure 5.7. The three-photon absorption results in the excitation of electrons from the valence to the conduction band via the trap states in the band gap.

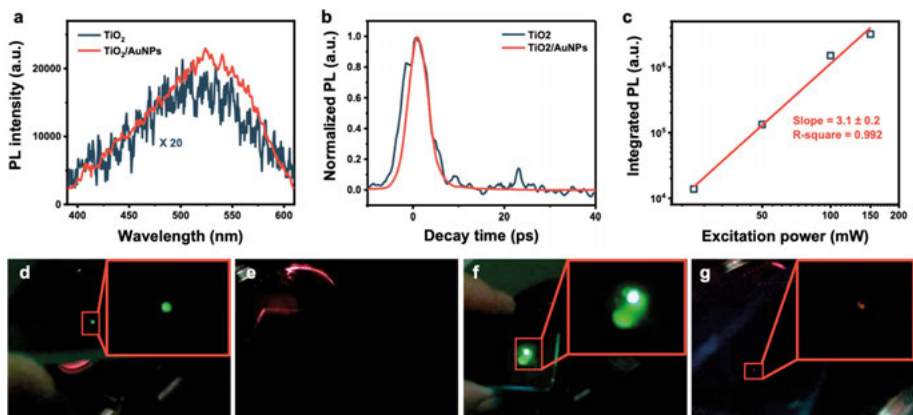


Figure 5.6. Transient photoluminescence studies: (a) comparison of the transient photoluminescence between TiO₂ and Au/TiO₂ after 800 nm excitation at room temperature, recorded with a streak camera, (b) kinetic traces of their emissions extracted at 525 nm, (c) dependence of the integrated photoluminescence intensity on the laser power intensity, and (d-g) photographs presenting the emission under 800 nm excitation from samples at different temperatures : (d) and (e) TiO₂ emission at 77 K and 295 K, (f) and (g) Au/TiO₂ emission at 77 K and 295 K. Note that the emission detected from Au/TiO₂ at 295 K is green, but the signal is too weak to be imaged.

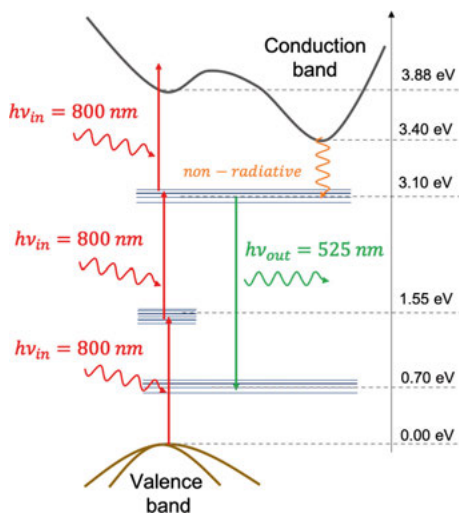


Figure 5.7. Level diagram describing the mechanism responsible for three-photon upconversion on TiO₂ involving three consecutive photon excitations of an electron from the valence band to the conduction band.

5.4 Conclusion

Herein, the Li-TFSI content in spiro-OMeTAD affects the plasmonic solar cell performance. The results revealed that the amount of oxidized spiro-OMeTAD (spiro⁺TFSI⁻) significantly conditioned device performance. The

optimal performance was obtained on a device with the spiro-OMeTAD layer containing around 33% spiro⁺TFSI⁻. TIRAS experiments suggested that both hot carriers are injected immediately and simultaneously after their formation, which was corroborated by the lack of hysteresis in the I-V curves. The fabricated DPSC can be made highly transparent, and their output power was found to be within what is required for low-power devices, such as IoT sensors and e-paper displays, according to Haight et al. [103].

Not only the hot carrier generation from the plasmonic nanoparticle but also the photonic effect on the absorption enhancement has potential applications in photoelectronic devices. I have shown that the addition of Au to TiO₂ increased its photon upconversion process by about 20 times. The process was found to require 3 photons, suggesting a climbing-the-ladder process i.e. successive excitation.

6. Summary and Outlook

Emerging photovoltaics have gained tremendous attention as innovative technologies for generating electricity from sunlight. They can be made from very thin layers of materials. The key aspect is new absorbing materials that generate free charge carriers efficiently. The research works presented in this thesis include two distinct materials: one is the wide-bandgap perovskite (FAPbBr_3) and another is the zero-bandgap plasmonic Au nanoparticle. Besides the absorbing layer, charge transport layers that selectively accept one type of charge carrier (electrons or holes) from the absorbing layer and facilitate charge extraction to the electrode are commonly employed in highly efficient solar cells, such as organic solar cells and perovskite solar cells. At the interface between these two layers, there are many factors to be considered such as energy level matching, the competition between charge injection and recombination, and stability issues. Currently, these novel solar cells have not yet been as widely used as traditional silicon solar cells. This thesis focuses on how interfaces and charge transport layers influence the charge injection and performance of solar cells.

In the FAPbBr_3 perovskite system (paper I and paper II), a laser with energy slightly above the bandgap was used to excite the perovskite material. The existence of free carriers and bounded excitons in FAPbBr_3 was identified by the time- and energy-resolved PL measurements under various laser powers. When FAPbBr_3 was attached to two electron transport materials, SnO_2 and TiO_2 , electron transfer happened. I found different photoluminescence quenching behaviors recorded by the streak camera. Interface with TiO_2 shows a higher electron transfer rate than SnO_2 which does not match that SnO_2 -based solar cell has better performance. According to the Marcus-Gerischer theory, the higher density of states in TiO_2 makes a difference. The improved overlap between the donor (FAPbBr_3) and the acceptor (TiO_2) promotes faster electron transfer. On the other hand, the superior conductivity of SnO_2 results in efficiently diffusing the injected charge, much more related to the solar cell efficiency. The findings provide an understanding that only photoluminescence (PL) quenching results could not indicate the solar cell performance. By changing the excitation density, analysis of the PL peak asymmetric broadening provides further information on the different transfers between free electrons and excitons.

To modify the energy levels of SnO_2 layer, KI was added. As the fermi level shifts up in the KI- SnO_2 film, the electron extraction behavior from excitons and free electrons changes, compared to the pure SnO_2 .

Unlike in semiconductors, the unique light-matter interaction in plasmonic systems enables high absorption and the generation of hot charge carriers. In systems containing plasmonic Au nanoparticles (paper III and paper IV), thin and compact TiO₂ functions as the electron transport layer. I tailored the solar cell performance by controlling the dopant (Li-TFSI) concentration in the spiro-OMeTAD hole transport material. The change is related to the amount of oxidized spiro-OMeTAD (spiro⁺TFSI⁻). The optimal performance was obtained on a device with the spiro-OMeTAD layer containing around 33% spiro⁺TFSI⁻. When measuring the direct plasmonic solar cell, I did not see the hysteresis behavior from the I-V curves. TIRAS experiments suggested that both hot carriers are injected immediately and simultaneously after their formation. Therefore, the accumulation of charge carriers at the interfaces does not take place in this new type of solar cell.

Also, the photonic effect of plasmonic nanoparticles on the absorption enhancement was explored. As the addition of Au to TiO₂, the photon up-conversion process was increased by about 20 times. The process was found to require 3 photons, suggesting a successive excitation mechanism. This is beneficial for photoelectronic applications.

The following parts are some prospects after reviewing my PhD studies.

As was aforementioned in Chapter 4, the TRPL measurements were carried out using a high laser power intensity, leading to very high photoexcited carrier densities (10^{18} cm^{-3}). However, under the steady-state AM 1.5G condition, the estimated carrier density only reaches $4 \times 10^{14} \text{ cm}^{-3}$ for high-quality methylammonium lead iodide (MAPbI₃) films with a monomolecular lifetime of 100 ns and in the absence of charge extraction [104]. To explore the charge dynamics at very low carrier densities, a highly sensitive transient absorption (TA) spectrometer was needed. A sensitivity level ($\Delta T/T$) of 10^{-7} was achieved by a novel technique of combining macropulse and micropulse and using a balanced detector scheme [105]. By means of the above-mentioned technique, a research work reported two fast-trapping processes in the Cs_{0.1}FA_{0.9}PbI₃ perovskite thin film from analyzing the charge carrier dynamics under solar illumination [106]. Future transient spectroscopy research with excitations close to solar illumination could give direct information on the photophysics of materials and the solar cell performance. An important factor to consider when incorporating a charge transport layer into devices is to avoid creating interfacial defects. The findings could guide further interfacial modifications toward highly efficient solar cells.

Recently, an experiment showed that one single photon can trigger photosynthesis in photosynthetic purple bacteria [107]. And, multiple exciton generation has also been observed in semiconductors [108]. As for the plasmonic nanoparticle, the question is how many hot electrons can be extracted when one photon excites one nanoparticle? Considering the future of plasmonic nanoparticles in solar cell applications, there are still a number of challenges that must be overcome. The obtained quantum efficiency of hot carrier injection

tion is far below the theoretical efficiency. One improvement could be realized by creating more rough interfaces. Another challenge is the spectral range of plasmonic nanoparticles. To increase the solar cell efficiency, more photons must be absorbed. One possible method is to fabricate a metal-semiconductor-nanoparticle structure to get a broadband absorber [109]. What's more, mixing different shapes of nanoparticles to cover a wide spectrum is also an option.

There may be some synergies in hybrid systems consisting of plasmonic nanoparticles and the perovskite semiconductor. In an example of Ag-CsPbBr₃ hybrid nanocrystals [110], the plasmon-induced hot electron and the resonant energy transfer processes coexist and are shown very high quantum efficiencies respectively. It is common to see many ideas based on incorporating plasmonic nanoparticles into the charge transport layers of various solar cells to reflect light and enhance the absorption of the active layer. Inserting the plasmonic nanoparticle directly into the absorbing layer could create some new phenomena.

7. Popular Scientific Summary

Rising global temperatures, melting ice and rising sea levels, extreme weather events including wildfires, hurricanes and typhoons, food shortages, and rising food prices, those environmental issues impact our lives. The root cause is climate change, which has received extensive coverage in the news. Efforts are underway to transition from fossil fuels to renewable energy sources and reduce and capture greenhouse gas emissions.

Sun shines brilliantly day after day. When the sunlight strikes Earth for just one hour, the delivered energy is more than the total global energy consumption over the span of an entire year. In addition to wind and hydropower, solar energy is viewed as one of the most promising solutions for generating sustainable energy. Solar cells play a crucial role in harnessing this energy by directly converting sunlight into electricity through the photovoltaic effect. In recent decades, silicon solar panels have been used to power street lighting systems, installed on rooftops to power households, and arranged over a considerable area, such as open fields and deserts, to build solar farms. However, high-purity silicon and energy-consuming fabrication processes limit the silicon solar cell to compete with other energy conversion devices. Some people also find that the opaque colors of silicon solar panels (black and bluish-black) are less aesthetically pleasing.

The basic operation of a solar cell involves several processes: when sunlight strikes the solar cell's surface, the photons are absorbed and the energy is transferred to electrons within the absorber layer. As a result, the electron is knocked loose and becomes free. The hole it leaves behind is positively charged. The efficient separation of the excited electrons from the holes is very important. Then, the separated electrons move towards the n-type (negative) charge transport layer while holes are directed to the p-type (positive) side. The flow of electrons creates an electric current.

The solar cell can be imagined as a system consisting of different machines and the connections between these form a whole. The mission is to move a ball through all the stations and deliver it to the destination. The challenge is to avoid dropping the ball during the transition at junctions. And the interaction is very important. However, the charge transfer in solar cells can be much faster than the resolution of human eyes, and a laser pulse is needed to observe this behavior.

Charge transfer processes occur in solar cells from femtosecond (10^{-15} s) to nanosecond (10^{-9} s) time scales, and understanding these processes is the key to designing and optimizing materials for high-performance solar cells.

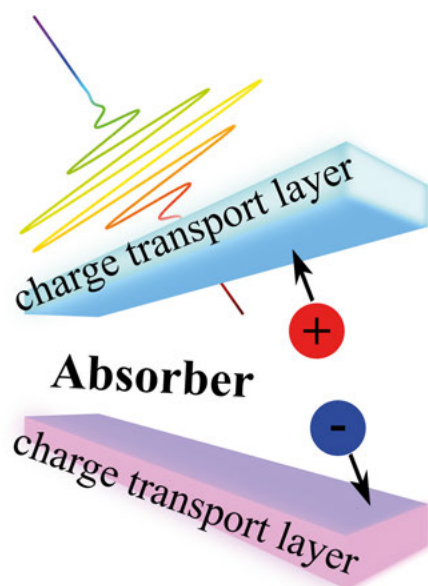


Figure 7.1. Simplified solar cell device under the laser pulse excitation.

Therefore, this thesis presents works on how electrons and holes transition from the absorber layer to the respective charge transport layers. Also, the properties of the charge transport layer show some impact on the solar cell performance. Firstly, the electron injection from a lead-bromide perovskite (FAPbBr_3) semiconductor to different metal oxide semiconductors was evaluated. The better interaction between two materials at the interface leads to faster electron injection. The material with higher conductivity ensures that injected electrons are pushed away more efficiently toward the next material layer. Both material properties should be considered when used in fabricating solar cells.

Another distinct absorber material, plasmonic gold nanoparticles, was used to fabricate transparent solar cells. The hole injection from the gold nanoparticle to organic semiconductors was evaluated. The dopant concentration in the organic semiconductor was altered to get an optimal output power of solar cells. There are some potential applications of such transparent solar cells such as building windows and mobile-phone screens.

8. Populärvetenskaplig Sammanfattning

Stigande globala temperaturer, smältande is och stigande havsnivåer, extremt väder med skogsbränder, orkaner och tyfoner, matbrist och stigande matpriser, dessa miljöproblem påverkar våra liv. Den grundläggande orsaken är klimatförändringar, som har fått omfattande täckning i nyheterna. Ansträngningar pågår för att övergå från fossila bränslen till förnybara energikällor och minska samt fånga upp växthusgasutsläpp.

Solen lyser strålade dag efter dag. När solljuset träffar jorden under bara en timme är den levererade energin mer än den totala globala energiförbrukningen under loppet av ett helt år. Förutom vind- och vattenkraft betraktas solenergi som en av de mest lovande lösningarna för att generera hållbar energi. Solceller spelar en avgörande roll för att utvinna denna energi genom att direkt omvandla solljus till elektricitet genom fotovoltaisk effekt. Under de senaste decennierna har kiselbaserade solpaneler använts för att driva gatubelysningsystem, installerats på tak för att förse hushåll med ström och arrangerats över omfattande områden, som öppna fält och öknar, för att bygga solkraftverk. Högren kisel och energikrävande tillverkningsprocesser begränsar dock kisel solceller från att konkurrera med andra energikonverteringsenheter. Vissa människor tycker också att de opaka färgerna på kiselpaneler (svart och blåsvart) är mindre estetiskt tilltalande.

Grundläggande funktionen av en solcell innefattar flera processer: När solljus träffar solcellens yta absorberas fotoner och energin överförs till elektroner inom absorberarlager. Som ett resultat lossnar elektronen och blir fri. Hålet den lämnar bakom sig är positivt laddat. En effektiv separation av de upphetade elektronerna från hålen är mycket viktig. Därefter rör sig de separerade elektronerna mot n-typ (negativ) laddningsöverföringslagret medan hålen riktar sig mot p-typ (positiv) sidan. Flödet av elektroner skapar en elektrisk ström.

Solcellen kan föreställas som ett system bestående av olika maskiner, och kopplingarna mellan dem bildar en helhet. Uppgiften är att förflytta en boll genom alla stationer och leverera den till destinationen. Utmaningen är att undvika att tappa bollen vid övergångarna i knutpunkterna. Och interaktionen är mycket viktig. Emellertid kan laddningsöverföringen i solceller vara mycket snabbare än människans ögon kan upplösa, och en laserpuls behövs för att observera detta beteende.

Laddningsöverföringsprocesser äger rum i solceller på tidskala från femtosekunder (10^{-15} s) till nanosekunder (10^{-9} s), och att förstå dessa processer är nyckeln till att designa och optimera material för högpresterande solceller. Därför presenterar denna avhandling arbeten om hur elektroner och hål övergår

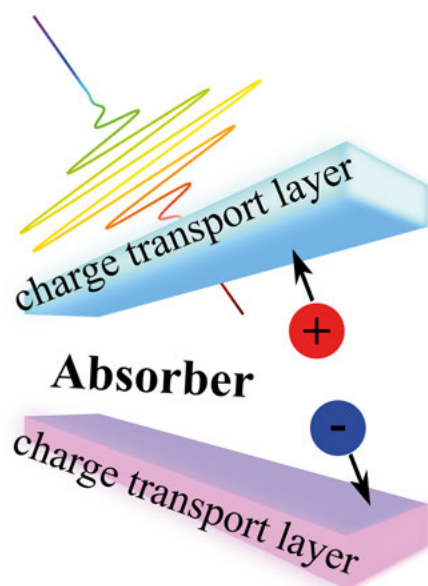


Figure 8.1. Förenklad solcellsenhet under laserpulsstimuleringen.

från absorberarlagret till de respektive laddningstransporterande lagren. Även egenskaperna hos laddningstransportlagret visar viss påverkan på solcellens prestanda. För det första utvärderades elektroninjektionen från en bly-bromid perovskit (FAPbBr_3) halvledare till olika metalloxidhalvledare. En bättre interaktionen mellan två material vid gränssnittet leder till snabbare elektroninjektion. Materialet med högre ledningsförmåga säkerställer att injicerade elektroner skjuts bort mer effektivt mot nästa materialsikt. Båda materialegenskaperna bör beaktas vid tillverkning av solceller.

En annan distinkt absorberingsmaterial, plasmoniska guld nanopartiklar, användes för att tillverka transparenta solceller. Hålinjektionen från guld nanopartikeln till organiska halvledare utvärderades. Dopantkoncentrationen i den organiska halvledaren ändrades för att uppnå en optimal utteffekt för solceller. Det finns några potentiella användningsområden för sådana transparenta solceller, så som byggnadsfönster och mobiltelefonskärmar.

9. Acknowledgements

I acknowledge the funding from the Swedish Energy Agency and the physical chemistry division of the Department of Chemistry-Ångström at Uppsala University for supporting my research.

First, I want to thank my supervisor Jacinto Sá for giving me the opportunity to join the nanoleaves group and driving me on in the research of plasmonics and transient spectroscopy. Also, I will never forget those philosophies on life that you told me, and believe these words will guide me to be a better person. Many thanks to my co-supervisors, Leif Hammarström and Tomas Edvinsson. I have always benefited from discussions and those scientific advice are invaluable. Jakob Thry, thanks for your expertise and patience when you gave me the training on Raman spectroscopy.

To our research group: Yocefu, thank you for welcoming me and sharing your experience at the beginning of my PhD study. You are a role model and a good scientist. Xianshao, Ananta, Robert, Vitor, Stylianos, Keely, and Pandiaraj, thanks for all the help with experiments and data fitting. Learning from you is extremely useful.

To the solar cell group: Erik M. J. Johansson and Gerrit Boschloo, Byeong Jo Kim, Malin Johansson, Fuxiang, Yawen, Hongling, Bowen, JiaJia, Aneta, Fiona, Anuja, Shipra, and Vishnu, thank you everyone for sharing the resources and facilitating the collaboration. I have broadened my knowledge during the group meetings. The working environment is really good.

Warm thanks to Sicong, Minli, Catherine, Hongwei, Min, Haoliang, Bin, Jingguo, Fangwen, Heyin, Chen, Aijie, Hua, and Huimin. All of you are brilliant in academics. I learned a lot from all of you and am really grateful for any suggestions you have given to me. I will always remember the gatherings, traveling, games, and sports as well.

I must thank Sree, David Moe, and Carlos Enrique with whom I shared office. It was a great pleasure being your office mate. I also want to thank Corentin and Jorn in the office next door. When my office is blocked, passing through your office is the only allowed way out. I enjoyed the amazing atmosphere on the 2nd floor and have always been encouraged. I am appreciative of the friendship.

I have enjoyed the interaction with colleagues on the ground floor. There are some people I want to mention. Starlar, you are kind and energetic. And I like the workout song you recommended. Nidhi, I appreciate your curious attitude and enthusiasm. Thanks, Martin for handing the Cary 5000 spectrophotometer instrument over to me. I had a lot of fun. Thanks to Andrew and Andrea for

handling the chemical waste together. Sigrid, thank you for organizing the Alumni Night seminars. I enjoyed it a lot and got many valuable information!

In addition, I would like to mention the present and past people from the Peafowl Plasmonics company. Qixiao, Henry, Laia, Mohamed Abdellah, Fei, Kari, and Matilda, thank you for the collaboration and discussions about solar cell devices. I look forward to seeing advanced solar cells fabricated by you.

I would also like to give my appreciation to Shili Zhang and Si Chen. The two courses that you are responsible for in the solid-state electronics division are fantastic. Zheqiang, thanks for your cooperation and discussion. I could not finish these courses without your help.

Leif Häggman and Sven Johansson, thanks for helping out, and maintaining and repairing instruments at the physical chemistry division.

Special thanks to my friends Yidong, Yibo, and Lin for the hospitality during my stays at Göteborg and Oslo. I enjoyed visiting you and had happy memories of our master's study. Zhen, thank you for the many phone calls despite the time zone difference. We have known each other for over 15 years and will continue sharing stories. It is you that reminds me of life outside the campus. Finally, I would like to give my deepest appreciation to my family. You always trust my decision and have supported me unconditionally. Thank you for providing me with the home, my sanctuary, for rest and relaxation. I love you truly.

References

- [1] Nikolay Belyakov. Chapter seventeen - solar energy. In *Sustainable Power Generation: Current Status, Future Challenges, and Perspectives*. Academic Press, 2019.
- [2] Jinyue Yan, Ying Yang, Pietro Elia Campana, and Jijiang He. City-level analysis of subsidy-free solar photovoltaic electricity price, profits, and grid parity in China. *Nature Energy*, 4(8):709–717, 2019.
- [3] Louise C. Hirst and Nicholas J. Ekins-Daukes. Fundamental losses in solar cells. *Progress in Photovoltaics: Research and Applications*, 19(3):286–293, 2011.
- [4] Best research-cell efficiency chart.
<https://www.nrel.gov/pv/cell-efficiency.html>.
- [5] Robert T. Ross and Arthur J. Nozik. Efficiency of hot-carrier solar energy converters. *Journal of Applied Physics*, 53(5):3813–3818, 1982.
- [6] Herbert Kroemer. Nobel lecture: Quasielectric fields and band offsets: teaching electrons new tricks. *Rev. Mod. Phys.*, 73:783–793, 2001.
- [7] Jacques I Pankove. *Optical processes in semiconductors*. Courier Corporation, 1975.
- [8] Karl W. Böer and Udo W. Pohl. *Optical Properties of Defects*, pages 629–676. Springer International Publishing, 2018.
- [9] Franz Urbach. The long-wavelength edge of photographic sensitivity and of the electronic absorption of solids. *Phys. Rev.*, 92:1324, 1953.
- [10] Giovanni Mannino, Ioannis Deretzis, Emanuele Smecca, Antonino La Magna, Alessandra Alberti, Davide Ceratti, and David Cahen. Temperature-dependent optical band gap in CsPbBr₃, MAPbBr₃, and FAPbBr₃ single crystals. *The Journal of Physical Chemistry Letters*, 11(7):2490–2496, 2020.
- [11] Mark (Anthony Mark) Fox. *Optical Properties of Solids*. Oxford master series in physics ; 3. Condensed matter physics. Oxford University Press, second edition, 2010.
- [12] Ajay Ram Srimath Kandada, Valerio D’Innocenzo, Guglielmo Lanzani, and Annamaria Petrozza. Photophysics of Hybrid Perovskites. In *Unconventional Thin Film Photovoltaics*. The Royal Society of Chemistry, 2016.
- [13] Johannes M. Richter, Federico Branchi, Franco Valduga de Almeida Camargo, Baodan Zhao, Richard H. Friend, Giulio Cerullo, and Felix Deschler. Ultrafast carrier thermalization in lead iodide perovskite probed with two-dimensional electronic spectroscopy. *Nature Communications*, 8(1):376, 2017.
- [14] Ivan Pelant and Jan Valenta. *Luminescence Spectroscopy of Semiconductors*. Oxford University Press, 2012.
- [15] Craig F Bohren and Donald R Huffman. *Absorption and scattering of light by small particles*. John Wiley & Sons, 1998.
- [16] Gregory V. Hartland. Optical studies of dynamics in noble metal nanostructures. *Chemical Reviews*, 111(6):3858–3887, 2011.

- [17] Julien R. G. Navarro and Martinus H. V. Werts. Resonant light scattering spectroscopy of gold, silver and gold-silver alloy nanoparticles and optical detection in microfluidic channels. *Analyst*, 138:583–592, 2013.
- [18] Matthieu Loumaigne, Clyde Midelet, Tristan Doussineau, Philippe Dugourd, Rodolphe Antoine, Meriem Stamboul, Anne Débarre, and Martinus H. V. Werts. Optical extinction and scattering cross sections of plasmonic nanoparticle dimers in aqueous suspension. *Nanoscale*, 8:6555–6570, 2016.
- [19] E. Dulkeith, T. Niedereichholz, T. A. Klar, J. Feldmann, G. von Plessen, D. I. Gittins, K. S. Mayya, and F. Caruso. Plasmon emission in photoexcited gold nanoparticles. *Phys. Rev. B*, 70:205424, 2004.
- [20] Xiaoguang Li, Di Xiao, and Zhenyu Zhang. Landau damping of quantum plasmons in metal nanostructures. *New Journal of Physics*, 15(2):023011, 2013.
- [21] Mark L. Brongersma, Naomi J. Halas, and Peter Nordlander. Plasmon-induced hot carrier science and technology. *Nature Nanotechnology*, 10(1):25–34, 2015.
- [22] M. Aeschlimann, M. Bauer, and S. Pawlik. Competing nonradiative channels for hot electron induced surface photochemistry. *Chemical Physics*, 205(1):127–141, 1996.
- [23] Gregory V. Hartland, Lucas V. Besteiro, Paul Johns, and Alexander O. Govorov. What’s so hot about electrons in metal nanoparticles ? *ACS Energy Letters*, 2(7):1641–1653, 2017.
- [24] R. N. Stuart, F. Wooten, and W. E. Spicer. Mean free path of hot electrons and holes in metals. *Phys. Rev. Lett.*, 10:7–9, 1963.
- [25] Ana M. Brown, Ravishankar Sundararaman, Prineha Narang, William A. III Goddard, and Harry A. Atwater. Nonradiative plasmon decay and hot carrier dynamics: Effects of phonons, surfaces, and geometry. *ACS Nano*, 10(1):957–966, 2016.
- [26] Qingxin Sun, Cheng Zhang, Weijia Shao, and Xiaofeng Li. Photodetection by hot electrons or hot holes: A comparable study on physics and performances. *ACS Omega*, 4(3):6020–6027, 2019.
- [27] César Clavero. Plasmon-induced hot-electron generation at nanoparticle/metal-oxide interfaces for photovoltaic and photocatalytic devices. *Nature Photonics*, 8(2):95–103, 2014.
- [28] T. Sakata, K. Hashimoto, and M. Hiramoto. New aspects of electron transfer on semiconductor surface: dye-sensitization system. *The Journal of Physical Chemistry*, 94(7):3040–3045, 1990.
- [29] David Stockwell, Ye Yang, Jier Huang, Chantelle Anfusio, Zhuangqun Huang, and Tianquan Lian. Comparison of electron-transfer dynamics from coumarin 343 to TiO₂, SnO₂, and ZnO nanocrystalline thin films: Role of interface-bound charge-separated pairs. *The Journal of Physical Chemistry C*, 114(14):6560–6566, 2010.
- [30] Kevin Tvrđy, Pavel A. Frantsuzov, and Prashant V. Kamat. Photoinduced electron transfer from semiconductor quantum dots to metal oxide nanoparticles. *Proceedings of the National Academy of Sciences*, 108(1):29–34, 2011.
- [31] Marco Ballabio and Enrique Cánovas. Electron transfer at quantum dot-metal

- oxide interfaces for solar energy conversion. *ACS Nanoscience Au*, 2(5):367–395, 2022.
- [32] M. Valenti, M. P. Jonsson, G. Biskos, A. Schmidt-Ott, and W. A. Smith. Plasmonic nanoparticle-semiconductor composites for efficient solar water splitting. *J. Mater. Chem. A*, 4:17891–17912, 2016.
- [33] Yuchao Zhang, Shuai He, Wenxiao Guo, Yue Hu, Jiawei Huang, Justin R. Mulcahy, and Wei David Wei. Surface-plasmon-driven hot electron photochemistry. *Chemical Reviews*, 118(6):2927–2954, 2018.
- [34] Yang Tian and Tetsu Tatsuma. Plasmon-induced photoelectrochemistry at metal nanoparticles supported on nanoporous TiO₂. *Chem. Commun.*, pages 1810–1811, 2004.
- [35] Mark W. Knight, Heidar Sobhani, Peter Nordlander, and Naomi J. Halas. Photodetection with active optical antennas. *Science*, 332(6030):702–704, 2011.
- [36] Andrew J. Leenheer, Prineha Narang, Nathan S. Lewis, and Harry A. Atwater. Solar energy conversion via hot electron internal photoemission in metallic nanostructures: Efficiency estimates. *Journal of Applied Physics*, 115(13):134301, 2014.
- [37] Yukina Takahashi and Tetsu Tatsuma. Solid state photovoltaic cells based on localized surface plasmon-induced charge separation. *Applied Physics Letters*, 99(18):182110, 2011.
- [38] Nianqiang Wu. Plasmonic metal-semiconductor photocatalysts and photoelectrochemical cells: a review. *Nanoscale*, 10:2679–2696, 2018.
- [39] K. Wu, J. Chen, J. R. McBride, and T. Lian. Efficient hot-electron transfer by a plasmon-induced interfacial charge-transfer transition. *Science*, 349(6248):632–635, 2015.
- [40] Run Long and Oleg V Prezhdo. Instantaneous generation of charge-separated state on TiO₂ surface sensitized with plasmonic nanoparticles. *Journal of the American Chemical Society*, 136(11):4343–4354, 2014.
- [41] Markus Lickleder, Reza Mohammadi, Nhat Truong Nguyen, Hyoungwon Park, Seyedsina Hejazi, Marcus Halik, Nicolas Vogel, Marco Altomare, and Patrik Schmuki. Dewetted Au nanoparticles on TiO₂ surfaces: Evidence of a size-independent plasmonic photoelectrochemical response. *The Journal of Physical Chemistry C*, 123(27):16934–16942, 2019.
- [42] Patrycja Makuła, Michał Pacia, and Wojciech Macyk. How to correctly determine the band gap energy of modified semiconductor photocatalysts based on UV-Vis spectra. *The Journal of Physical Chemistry Letters*, 9(23):6814–6817, 2018.
- [43] Hamamatsu Photonics K.K. Guide to streak cameras. 2008.
- [44] Jan Obrzut and Kirt A. Page. Electrical conductivity and relaxation in poly(3-hexylthiophene). *Phys. Rev. B*, 80:195211, 2009.
- [45] Fabian C. Hanusch, Erwin Wiesenmayer, Eric Mankel, Andreas Binek, Philipp Angloher, Christina Fraunhofer, Naja Giesbrecht, Johann M. Feckl, Wolfram Jaegermann, Dirk Johrendt, Thomas Bein, and Pablo Docampo. Efficient planar heterojunction perovskite solar cells based on formamidinium lead bromide. *The Journal of Physical Chemistry Letters*, 5(16):2791–2795, 2014.
- [46] Yawen Liu, Byeong Jo Kim, Hua Wu, Gerrit Boschloo, and Erik M. J.

- Johansson. Efficient and stable FAPbBr₃ perovskite solar cells via interface modification by a low-dimensional perovskite layer. *ACS Applied Energy Materials*, 4(9):9276–9282, 2021.
- [47] Yongfei Zhang, Yongqi Liang, Yajuan Wang, Fengwan Guo, Licheng Sun, and Dongsheng Xu. Planar FAPbBr₃ solar cells with power conversion efficiency above 10%. *ACS Energy Letters*, 3(8):1808–1814, 2018.
- [48] Huifen Xu, Zheng Liang, Jiajiu Ye, Shendong Xu, Zihan Wang, Liangzheng Zhu, Xiaojing Chen, Zhengguo Xiao, Xu Pan, and Guozhen Liu. Guanidinium-assisted crystallization modulation and reduction of open-circuit voltage deficit for efficient planar FAPbBr₃ perovskite solar cells. *Chemical Engineering Journal*, 437:135181, 2022.
- [49] Chengbo Li, Aili Wang, Xiaoyu Deng, Shurong Wang, Yuan Yuan, Liming Ding, and Feng Hao. Insights into ultrafast carrier dynamics in perovskite thin films and solar cells. *ACS Photonics*, 7(8):1893–1907, 2020.
- [50] Carlito S. Jr. Ponseca, Tom J. Savenije, Mohamed Abdellah, Kaibo Zheng, Arkady Yartsev, Tobjörn Pascher, Tobias Harlang, Pavel Chabera, Tõnu Pullerits, Andrey Stepanov, Jean-Pierre Wolf, and Villy Sundström. Organometal halide perovskite solar cell materials rationalized: Ultrafast charge generation, high and microsecond-long balanced mobilities, and slow recombination. *Journal of the American Chemical Society*, 136(14):5189–5192, 2014.
- [51] Jiangjian Shi, Dongmei Li, Yanhong Luo, Huijue Wu, and Qingbo Meng. Opto-electro-modulated transient photovoltage and photocurrent system for investigation of charge transport and recombination in solar cells. *Review of Scientific Instruments*, 87(12):123107, 2016.
- [52] James M. Ball and Annamaria Petrozza. Defects in perovskite-halides and their effects in solar cells. *Nature Energy*, 1(11):16149, 2016.
- [53] Katelyn P. Goetz, Alexander D. Taylor, Fabian Paulus, and Yana Vaynzof. Shining light on the photoluminescence properties of metal halide perovskites. *Advanced Functional Materials*, 30(23):1910004, 2020.
- [54] Christopher L Davies, Marina R Filip, Jay B Patel, Timothy W Crothers, Carla Verdi, Adam D Wright, Rebecca L Milot, Feliciano Giustino, Michael B Johnston, and Laura M Herz. Bimolecular recombination in methylammonium lead triiodide perovskite is an inverse absorption process. *Nature communications*, 9(1):293, 2018.
- [55] Supriya Ghosh, Qi Shi, Bapi Pradhan, Pushpendra Kumar, Zhengjun Wang, Somobrata Acharya, Suman Kalyan Pal, Tõnu Pullerits, and Khadga J. Karki. Phonon coupling with excitons and free carriers in formamidinium lead bromide perovskite nanocrystals. *The Journal of Physical Chemistry Letters*, 9(15):4245–4250, 2018.
- [56] Zhaoliang Yang, Xiaomin Wang, Yuzhong Chen, Zhenfa Zheng, Zeng Chen, Wenqi Xu, Weimin Liu, Yang Yang, Jin Zhao, Tao Chen, et al. Ultrafast self-trapping of photoexcited carriers sets the upper limit on antimony trisulfide photovoltaic devices. *Nature Communications*, 10(1):4540, 2019.
- [57] Nikolaos Droseros, Giulia Longo, Jan C. Brauer, Michele Sessolo, Henk J. Bolink, and Natalie Banerji. Origin of the enhanced photoluminescence quantum yield in MAPbBr₃ perovskite with reduced crystal size. *ACS Energy*

- Letters*, 3(6):1458–1466, 2018.
- [58] Harshita Bhatia, Biplab Ghosh, and Elke Debroye. Colloidal FAPbBr₃ perovskite nanocrystals for light emission: what’s going on? *J. Mater. Chem. C*, 10:13437–13461, 2022.
 - [59] Chen Hu, Sunil B Shivarudraiah, Herman HY Sung, Ian D Williams, Jonathan E Halpert, and Shihe Yang. Discovery of a new intermediate enables one-step deposition of high-quality perovskite films via solvent engineering. *Solar RRL*, 5(4):2000712, 2021.
 - [60] Konstantin Schötz, Abdelrahman M. Askar, Wei Peng, Dominik Seeberger, Tanaji P. Gujar, Mukundan Thelakkat, Anna Köhler, Sven Huettnner, Osman M. Bakr, Karthik Shankar, and Fabian Panzer. Double peak emission in lead halide perovskites by self-absorption. *J. Mater. Chem. C*, 8:2289–2300, 2020.
 - [61] Michal Baranowski and Paulina Plochocka. Excitons in metal-halide perovskites. *Advanced Energy Materials*, 10(26):1903659, 2020.
 - [62] Manjari Jain, Deepika Gill, Preeti Bhumla, Pooja Basera, and Saswata Bhattacharya. Theoretical insights to excitonic effect in lead bromide perovskites. *Applied Physics Letters*, 118(19):192103, 2021.
 - [63] Krzysztof Galkowski, Anatolie Mitiglu, Atsuhiko Miyata, Paulina Plochocka, Oliver Portugall, Giles E. Eperon, Jacob Tse-Wei Wang, Thomas Stergiopoulos, Samuel D. Stranks, Henry J. Snaith, and Robin J. Nicholas. Determination of the exciton binding energy and effective masses for methylammonium and formamidinium lead tri-halide perovskite semiconductors. *Energy Environ. Sci.*, 9:962–970, 2016.
 - [64] Mingjie Li, Raihana Begum, Jianhui Fu, Qiang Xu, Teck Ming Koh, Sjoerd A. Veldhuis, Michael Grätzel, Nripan Mathews, Subodh Mhaisalkar, and Tze Chien Sum. Low threshold and efficient multiple exciton generation in halide perovskite nanocrystals. *Nature Communications*, 9(1):4197, 2018.
 - [65] Samuel D. Stranks, Giles E. Eperon, Giulia Grancini, Christopher Menelaou, Marcelo J. P. Alcocer, Tomas Leijtens, Laura M. Herz, Annamaria Petrozza, and Henry J. Snaith. Electron-hole diffusion lengths exceeding 1 micrometer in an organometal trihalide perovskite absorber. *Science*, 342(6156):341–344, 2013.
 - [66] Guichuan Xing, Nripan Mathews, Shuangyong Sun, Swee Sien Lim, Yeng Ming Lam, Michael Grätzel, Subodh Mhaisalkar, and Tze Chien Sum. Long-range balanced electron- and hole-transport lengths in organic-inorganic CH₃NH₃PbI₃. *Science*, 342(6156):344–347, 2013.
 - [67] Ayan A. Zhumekenov, Makhsud I. Saidaminov, Md Azimul Haque, Erkki Alarousu, Smritakshi Phukan Sarmah, Banavoth Murali, Ibrahim Dursun, Xiao-He Miao, Ahmed L. Abdelhady, Tom Wu, Omar F. Mohammed, and Osman M. Bakr. Formamidinium lead halide perovskite crystals with unprecedented long carrier dynamics and diffusion length. *ACS Energy Letters*, 1(1):32–37, 2016.
 - [68] Valerio D’Innocenzo, Giulia Grancini, Marcelo J. P. Alcocer, Ajay Ram Srimath Kandada, Samuel D. Stranks, Michael M. Lee, Guglielmo Lanzani, Henry J. Snaith, and Annamaria Petrozza. Excitons versus free charges in organo-lead tri-halide perovskites. *Nature Communications*, 5:3586, 2014.

- [69] J. Takeda, H. Jinnouchi, S. Kurita, Y.F. Chen, and T. Yao. Dynamics of photoexcited high density carriers in ZnO epitaxial thin films. *Physica Status Solidi (B)*, 229(2):877–880, 2002.
- [70] T. Shih, E. Mazur, J.-P. Richters, J. Gutowski, and T. Voss. Ultrafast exciton dynamics in ZnO: Excitonic versus electron-hole plasma lasing. *Journal of Applied Physics*, 109(4):043504–043504–5, 2011.
- [71] Jinhyun Kim, Robert Godin, Stoichko D. Dimitrov, Tian Du, Daniel Bryant, Martyn A. McLachlan, and James R. Durrant. Excitation density dependent photoluminescence quenching and charge transfer efficiencies in hybrid perovskite/organic semiconductor bilayers. *Advanced Energy Materials*, 8(35):1802474, 2018.
- [72] Ajay Perumal, Sushant Shendre, Mingjie Li, Yong Kang Eugene Tay, Vijay Kumar Sharma, Shi Chen, Zhanhua Wei, Qing Liu, Yuan Gao, Pio John S. Buenconsejo, Swee Tiam Tan, Chee Lip Gan, Qihua Xiong, Tze Chien Sum, and Hilmi Volkan Demir. High brightness formamidinium lead bromide perovskite nanocrystal light emitting devices. *Scientific Reports*, 6(1):36733, 2016.
- [73] Yanqing Zu, Jun Xi, Lu Li, Jinfei Dai, Shuangpeng Wang, Feng Yun, Bo Jiao, Hua Dong, Xun Hou, and Zhaoxin Wu. High-brightness and color-tunable FAPbBr₃ perovskite nanocrystals 2.0 enable ultrapure green luminescence for achieving recommendation 2020 displays. *ACS Applied Materials & Interfaces*, 12(2):2835–2841, 2020.
- [74] Priti Tiwana, Pablo Docampo, Michael B. Johnston, Henry J. Snaith, and Laura M. Herz. Electron mobility and injection dynamics in mesoporous ZnO, SnO₂, and TiO₂ films used in dye-sensitized solar cells. *ACS Nano*, 5(6):5158–5166, 2011.
- [75] Qi Jiang, Liuqi Zhang, Haolin Wang, Xiaolei Yang, Junhua Meng, Heng Liu, Zhigang Yin, Jinliang Wu, Xingwang Zhang, and Jingbi You. Enhanced electron extraction using SnO₂ for high-efficiency planar-structure HC(NH₂)₂PbI₃-based perovskite solar cells. *Nature Energy*, 2(1):16177, 2016.
- [76] Jason J. Yoo, Gabkyung Seo, Matthew R. Chua, Tae Gwan Park, Yongli Lu, Fabian Rotermund, Young-Ki Kim, Chan Su Moon, Nam Joong Jeon, Juan-Pablo Correa-Baena, Vladimir Bulović, Seong Sik Shin, Mouni G. Bawendi, and Jangwon Seo. Efficient perovskite solar cells via improved carrier management. *Nature*, 590(7847):587–593, 2021.
- [77] So Yeon Park and Kai Zhu. Advances in SnO₂ for efficient and stable n-i-p perovskite solar cells. *Advanced Materials*, 34(27):2110438, 2022.
- [78] R. A. Marcus. On the theory of oxidation-reduction reactions involving electron transfer. I. *The Journal of chemical physics*, 24(5):966–978, 1956.
- [79] Juan Pablo Correa Baena, Ludmilla Steier, Wolfgang Tress, Michael Saliba, Stefanie Neutzner, Taisuke Matsui, Fabrizio Giordano, T. Jesper Jacobsson, Ajay Ram Srimath Kandada, Shaik M. Zakeeruddin, Annamaria Petrozza, Antonio Abate, Mohammad Khaja Nazeeruddin, Michael Grätzel, and Anders Hagfeldt. Highly efficient planar perovskite solar cells through band alignment engineering. *Energy Environ. Sci.*, 8:2928–2934, 2015.
- [80] Rüdiger Memming. *Electron Transfer Theories*, chapter 6, pages 127–168. John Wiley & Sons, Ltd, 2015.

- [81] Maofeng Dou and Clas Persson. Comparative study of rutile and anatase SnO_2 and TiO_2 : Band-edge structures, dielectric functions, and polaron effects. *Journal of Applied Physics*, 113(8):083703, 2013.
- [82] Yocef Hattori, Sol Gutiérrez Álvarez, Jie Meng, Kaibo Zheng, and Jacinto Sá. Role of the metal oxide electron acceptor on gold-plasmon hot-carrier dynamics and its implication to photocatalysis and photovoltaics. *ACS Applied Nano Materials*, 4(2):2052–2060, 2021.
- [83] Wanchun Xiang, Shengzhong (Frank) Liu, and Wolfgang Tress. Interfaces and interfacial layers in inorganic perovskite solar cells. *Angewandte Chemie International Edition*, 60(51):26440–26453, 2021.
- [84] Xu Liu, Yuanfang Zhang, Lei Shi, Ziheng Liu, Jialiang Huang, Jae Sung Yun, Yiyu Zeng, Aobo Pu, Kaiwen Sun, Ziv Hameiri, John A. Stride, Jan Seidel, Martin A. Green, and Xiaojing Hao. Exploring inorganic binary alkaline halide to passivate defects in low-temperature-processed planar-structure hybrid perovskite solar cells. *Advanced Energy Materials*, 8(20):1800138, 2018.
- [85] Ning Zhu, Xin Qi, Yuqing Zhang, Ganghong Liu, Cuncun Wu, Duo Wang, Xuan Guo, Wei Luo, Xiangdong Li, Haozhe Hu, Zhijian Chen, Lixin Xiao, and Bo Qu. High efficiency (18.53%) of flexible perovskite solar cells via the insertion of potassium chloride between SnO_2 and $\text{CH}_3\text{NH}_3\text{PbI}_3$ layers. *ACS Applied Energy Materials*, 2(5):3676–3682, 2019.
- [86] Janardan Dagar, Katrin Hirslandt, Aboma Merdasa, Aniela Czudek, Rahim Munir, Fengshuo Zu, Norbert Koch, Thomas Dittrich, and Eva L. Unger. Alkali salts as interface modifiers in n-i-p hybrid perovskite solar cells. *Solar RRL*, 3(9):1900088, 2019.
- [87] Tongle Bu, Jing Li, Fei Zheng, Weijian Chen, Xiaoming Wen, Zhiliang Ku, Yong Peng, Jie Zhong, Yi-Bing Cheng, and Fuzhi Huang. Universal passivation strategy to slot-die printed SnO_2 for hysteresis-free efficient flexible perovskite solar module. *Nature Communications*, 9(1):4609, 2018.
- [88] SeongYeon Kim, Fei Zhang, Jinhui Tong, Xihan Chen, Enkhjargal Enkhbayar, Kai Zhu, and JunHo Kim. Effects of potassium treatment on SnO_2 electron transport layers for improvements of perovskite solar cells. *Solar Energy*, 233:353–362, 2022.
- [89] Rui Zhao, Zhiqiang Deng, Zequn Zhang, Jing Zhang, Tonghui Guo, Yanjun Xing, Xiaohui Liu, Like Huang, Ziyang Hu, and Yuejin Zhu. Alkali metal cations modulate the energy level of SnO_2 via micro-agglomerating and anchoring for perovskite solar cells. *ACS Applied Materials & Interfaces*, 14(32):36711–36720, 2022.
- [90] SeongYeon Kim, Fei Zhang, Jinhui Tong, Xihan Chen, Enkhjargal Enkhbayar, Kai Zhu, and JunHo Kim. Effects of potassium treatment on SnO_2 electron transport layers for improvements of perovskite solar cells. *Solar Energy*, 233:353–362, 2022.
- [91] Takashi Minemoto and Masashi Murata. Theoretical analysis on effect of band offsets in perovskite solar cells. *Solar Energy Materials and Solar Cells*, 133:8–14, 2015.
- [92] Eline M. Hutter, Thomas Kirchartz, Bruno Ehrler, David Cahen, and Elizabeth von Hauff. Pitfalls and prospects of optical spectroscopy to characterize perovskite-transport layer interfaces. *Applied Physics Letters*,

- 116(10):100501, 2020.
- [93] Yang Tian and Tetsu Tatsuma. Mechanisms and applications of plasmon-induced charge separation at TiO_2 films loaded with gold nanoparticles. *Journal of the American Chemical Society*, 127(20):7632–7637, 2005.
 - [94] Kefeng YU, Nobuyuki SAKAI, and Tetsu TATSUMA. Plasmon resonance-based solid-state photovoltaic devices. *Electrochemistry*, 76(2):161–164, 2008.
 - [95] Fuming Wang and Nicholas A. Melosh. Plasmonic energy collection through hot carrier extraction. *Nano Letters*, 11(12):5426–5430, 2011.
 - [96] Philipp Reineck, George P. Lee, Delia Brick, Matthias Karg, Paul Mulvaney, and Udo Bach. A solid-state plasmonic solar cell via metal nanoparticle self-assembly. *Advanced Materials*, 24(35):4750–4755, 2012.
 - [97] Simona Fantacci, Filippo De Angelis, Mohammad K. Nazeeruddin, and Michael Grätzel. Electronic and optical properties of the Spiro–MeOTAD hole conductor in its neutral and oxidized forms: A DFT/TDDFT investigation. *The Journal of Physical Chemistry C*, 115(46):23126–23133, 2011.
 - [98] Henry J. Snaith and Michael Grätzel. Enhanced charge mobility in a molecular hole transporter via addition of redox inactive ionic dopant: Implication to dye-sensitized solar cells. *Applied Physics Letters*, 89(26):262114, 2006.
 - [99] Antonio Abate, Tomas Leijtens, Sandeep Pathak, Joël Teuscher, Roberto Avolio, Maria E. Errico, James Kirkpatrick, James M. Ball, Pablo Docampo, Ian McPherson, and Henry J. Snaith. Lithium salts as "redox active" p-type dopants for organic semiconductors and their impact in solid-state dye-sensitized solar cells. *Phys. Chem. Chem. Phys.*, 15:2572–2579, 2013.
 - [100] Philipp Reineck, Delia Brick, Paul Mulvaney, and Udo Bach. Plasmonic hot electron solar cells: The effect of nanoparticle size on quantum efficiency. *The Journal of Physical Chemistry Letters*, 7(20):4137–4141, 2016.
 - [101] K. E. A. Hooper, H. K. H. Lee, M. J. Newman, S. Meroni, J. Baker, T. M. Watson, and W. C. Tsoi. Probing the degradation and homogeneity of embedded perovskite semiconducting layers in photovoltaic devices by raman spectroscopy. *Phys. Chem. Chem. Phys.*, 19:5246–5253, 2017.
 - [102] Francesco Lamberti, Teresa Gatti, Enrico Cescon, Roberto Sorrentino, Antonio Rizzo, Enzo Menna, Gaudenzio Meneghesso, Moreno Meneghetti, Annamaria Petrozza, and Lorenzo Franco. Evidence of Spiro–OMeTAD de-doping by tert-butylpyridine additive in hole-transporting layers for perovskite solar cells. *Chem*, 5(7):1806–1817, 2019.
 - [103] Richard Haight, Wilfried Haensch, and Daniel Friedman. Solar-powering the internet of things. *Science*, 353(6295):124–125, 2016.
 - [104] Michael B. Johnston and Laura M. Herz. Hybrid perovskites for photovoltaics: Charge-carrier recombination, diffusion, and radiative efficiencies. *Accounts of Chemical Research*, 49(1):146–154, 2016.
 - [105] Huang Li, Gang Hu, Bo-Han Li, Wen Zeng, Jingquan Zhang, Xingan Wang, Chuanyao Zhou, Zefeng Ren, and Xueming Yang. Ultrahigh sensitive transient absorption spectrometer. *Review of Scientific Instruments*, 92(5):053002, 2021.
 - [106] Bo-Han Li, Huang Li, Haipeng Di, Zhipeng Xuan, Wen Zeng, Jia-Cheng Wang, Da-Bing Cheng, Chuanyao Zhou, Xingan Wang, Yiyang Zhao, Jingquan

- Zhang, Zefeng Ren, and Xueming Yang. Probing the genuine carrier dynamics of semiconducting perovskites under sunlight. *JACS Au*, 3(2):441–448, 2023.
- [107] Quanwei Li, Kaydren Orcutt, Robert L. Cook, Javier Sabines-Chesterking, Ashley L. Tong, Gabriela S. Schlau-Cohen, Xiang Zhang, Graham R. Fleming, and K. Birgitta Whaley. Single-photon absorption and emission from a natural photosynthetic complex. *Nature*, 619(7969):300–304, 2023.
- [108] Matthew C. Beard. Multiple exciton generation in semiconductor quantum dots. *The Journal of Physical Chemistry Letters*, 2(11):1282–1288, 2011.
- [109] Charlene Ng, Jasper J. Cadusch, Svetlana Dligatch, Ann Roberts, Timothy J. Davis, Paul Mulvaney, and Daniel E. Gómez. Hot carrier extraction with plasmonic broadband absorbers. *ACS Nano*, 10(4):4704–4711, 2016.
- [110] Xinyu Huang, Hongbo Li, Chunfeng Zhang, Shijing Tan, Zhangzhang Chen, Lan Chen, Zhenda Lu, Xiaoyong Wang, and Min Xiao. Efficient plasmon-hot electron conversion in Ag-CsPbBr₃ hybrid nanocrystals. *Nature Communications*, 10(1):1163, 2019.

Acta Universitatis Upsaliensis

Digital Comprehensive Summaries of Uppsala Dissertations from the Faculty of Science and Technology 2308

Editor: The Dean of the Faculty of Science and Technology

A doctoral dissertation from the Faculty of Science and Technology, Uppsala University, is usually a summary of a number of papers. A few copies of the complete dissertation are kept at major Swedish research libraries, while the summary alone is distributed internationally through the series Digital Comprehensive Summaries of Uppsala Dissertations from the Faculty of Science and Technology. (Prior to January, 2005, the series was published under the title "Comprehensive Summaries of Uppsala Dissertations from the Faculty of Science and Technology".)



Distribution: publications.uu.se
urn:nbn:se:uu:diva-512175

ACTA UNIVERSITATIS
UPSALIENSIS
2023